



Effect of Ti^{4+} on the structure of nepheline (NaAlSiO_4) glass

Emily T Nienhuis, José Marcial, Thibaut Robine, Charles Le Losq, Daniel R. Neuville, Martin C Stennett, Neil C Hyatt, John S Mccloy

► To cite this version:

Emily T Nienhuis, José Marcial, Thibaut Robine, Charles Le Losq, Daniel R. Neuville, et al.. Effect of Ti^{4+} on the structure of nepheline (NaAlSiO_4) glass. *Geochimica et Cosmochimica Acta*, 2020, 290, pp.333-351. 10.1016/j.gca.2020.09.015 . hal-02989507

HAL Id: hal-02989507

<https://hal.science/hal-02989507>

Submitted on 12 Nov 2020

HAL is a multi-disciplinary open access archive for the deposit and dissemination of scientific research documents, whether they are published or not. The documents may come from teaching and research institutions in France or abroad, or from public or private research centers.

L'archive ouverte pluridisciplinaire **HAL**, est destinée au dépôt et à la diffusion de documents scientifiques de niveau recherche, publiés ou non, émanant des établissements d'enseignement et de recherche français ou étrangers, des laboratoires publics ou privés.

Effect of Ti^{4+} on the Structure of Nepheline (NaAlSiO_4) Glass

Emily T. Nienhuis,¹ José Marcial,^{2,3} Thibaut Robine,⁴ Charles Le Losq,⁴ Daniel R. Neuville,⁴
Martin C. Stennett,⁵ Neil C. Hyatt,⁵ John S. McCloy^{1,2,3,4,5}

¹Materials Science and Engineering Program, Washington State University, PO Box 641030, Pullman,
WA, 99164-1030

²Pacific Northwest National Laboratory, Richland, WA 99352

³School of Mechanical and Materials Engineering, Washington State University, PO BOX 642920,
Pullman, WA 99164-2920

⁴Géomatériaux, CNRS, Institut de Physique du Globe de Paris, USPC, 1 rue Jussieu, 75252 Paris Cedex
05, France

⁵Department of Materials Science and Engineering, The University of Sheffield, Sir Robert Hadfield
Building, Mappin Street, Sheffield, S1 3JD, UK

Corresponding Author: John McCloy john.mccloy@wsu.edu

Abstract

In this study, the effect of Ti^{4+} on the structure of nepheline glass (NaAlSiO_4) is investigated as SiO_2 is systematically replaced with TiO_2 . Traditionally, TiO_2 is considered to be a nucleating agent for silicate crystallization but can also be incorporated into the glass network in relatively large amounts as either a glass former or modifier depending on its coordination with oxygen. To determine the effect of Ti^{4+} on the structure of nepheline glass, X-ray and neutron pair distribution function (PDF) analysis paired with Empirical Potential Structure Refinement (EPSR) were conducted and are supplemented with Raman spectroscopy and Ti K-edge X-ray absorption spectroscopy (including Extended X-ray Absorption Fine Structure, EXAFS). Through these methods, it has been found that up to 15 mol% (16 wt%) TiO_2 can incorporate into the glass network as a primarily four-fold coordinated species, with a minor contribution of five-fold coordinated Ti as the TiO_2 content is increased. Between $\text{NaAlTi}_{0.1}\text{Si}_{0.9}\text{O}_4$ and $\text{NaAlTi}_{0.2}\text{Si}_{0.8}\text{O}_4$, EXAFS suggests a local structure change in the second nearest neighbor, from a Ti atom to an Al atom. Raman spectroscopy also suggests that as Ti content increases, the Na environment becomes more ordered.

1.0 Introduction

Titania (TiO_2) has been found to play a significant role in nearly all glass families, though it is not considered to be a glass-forming oxide on its own. Glass formation for Ti^{4+} -containing systems has been reported for the following glass families: alkali silicate (Gan et al., 1996; Hamilton and Cleek, 1958; Henderson and St-Amour, 2004; Limbach et al., 2017; Yarker et al., 1986), alkaline earth silicate (Gan et al., 1996; Henderson and St-Amour, 2004; Limbach et al., 2017), aluminosilicate (Kajiwarra, 1988), other silicate based glasses (Peterson and Kurkjian, 1972), borate (Lee et al., 2012), tellurite (Nasu et al., 1990; Sabadel et al., 1997), and phosphate (Fu, 2011; Hoppe et al., 2007), as well as in alkali-titanate glasses without traditional glass-forming oxides (Miyaji et al., 1991; Rao, 1964; Sakka et al., 1990; Sakka et al., 1989). For many of these glasses, discerning the local environment of Ti^{4+} was a primary feature of the study, and was related to the role of Ti^{4+} within the glass network, whether it be a glass-former, glass-modifier, or an intermediate species. Unless otherwise noted, the subsequent discussion refers to Ti^{4+} .

In glasses, Ti has been observed to be four-, five-, and six-fold coordinated with oxygen, and its role within the glass network is dependent upon its coordination state. Four-fold coordinated Ti, $^{[4]}\text{Ti}$, is largely considered to act as a glass former, whereas six-fold coordinated Ti, $^{[6]}\text{Ti}$, acts as a modifier (Mysen and Neuville, 1995). Five-fold coordinated Ti, $^{[5]}\text{Ti}$, is hypothesized to act as both a network modifier and a network former due to two distinct types of bonds with oxygen – one capable of forming bridging oxygen bonds and the other a terminal oxygen bond (Farges et al., 1996b; Henderson and St-Amour, 2004). More recently, though, $^{[5]}\text{Ti}$ has been described primarily as a network former due to its ability to form bridging oxygen with other network forming species within the glass, despite the presence of the terminal oxygen bond

(Henderson and St-Amour, 2004; Limbach et al., 2017). Most studies interested in the local structure of Ti within glasses have concluded that the coordination of Ti is dependent on the glass composition and the overall concentration of Ti within the glass, and often a mixture of two coordination states is reported. This mixture of coordination states can result in Ti occupying two distinct sites within the glass network. This is referred to as the “two-site model” by Greigor et al (Greigor et al., 1983) and is discussed in terms of the “dual role of titanium” by Rao et al (Rao, 1963), and is seen as an equilibrium between the two coordination states.

Overall, increased amounts of TiO_2 can be incorporated into glasses containing alkali and alkaline earth oxides as compared with those containing only silica (Gan et al., 1996; Limbach et al., 2017; Yarker et al., 1986). It has also been observed that Ti is five-fold coordinated at relatively low concentrations, and then shifts to $^{[4]}\text{Ti}$ before forming octahedral $^{[6]}\text{Ti}$ and then crystallizing (Greigor et al., 1983; Henderson and St-Amour, 2004). The relative amount of TiO_2 that can be accepted into the glass structure and the Ti coordination are hypothesized to be related by two factors, network rigidity and the amount of free-volume within the network (which must be sufficiently large to accommodate Ti polyhedra of various sizes) (Henderson and Fleet, 1997; Williams et al., 2019). Based upon this, $^{[4]}\text{Ti}$ is likely to be present in an unconstrained network featuring non-bridging oxygen, whereas $^{[5]}\text{Ti}$ is likely to be observed in a more connected and constrained glass network. $^{[6]}\text{Ti}$ results from volume constraints within the glass network, whether it be a Ti-containing silicate or an alkali/alkaline earth silicate glass.

In the case of glasses containing only TiO_2 and SiO_2 , at low TiO_2 additions, the network is primarily made up of SiO_2 with bridging oxygen, yielding a relatively rigid network. As TiO_2 is added, it serves to alter the network connectivity promoting the formation of $^{[4]}\text{Ti}$, through the initial presence of $^{[5]}\text{Ti}$ acting as a modifier to break up the network. In glasses containing alkali

or alkaline earth oxides, the network is broken up by network modifiers, and non-bridging oxygens are present, which does not necessarily require the initial presence of $^{[5]}\text{Ti}$ as the TiO_2 - SiO_2 glasses do.

Additionally, studies of molten TiO_2 have observed five-fold coordinated Ti (Alderman et al., 2014) while crystalline TiO_2 polymorphs (anatase, brookite, and rutile) have six-fold coordinated Ti present as $^{[6]}\text{Ti}$ octahedra (Hess et al., 2001; Krawczynski et al., 2009; Krzmann et al., 2012; Yu et al., 2009).

Ti is also found in more complex natural glasses on the order of ~1 wt% (for example, tektites and some basaltic glasses) and up to ~16 wt% in lunar glasses (Cicconi and Neuville, 2019), though in lunar glasses, Ti can be present as Ti^{3+} due to low oxygen fugacity (Krawczynski et al., 2009). Additionally, fulgurites formed in mafic or ultramafic rock can have increased amounts of TiO_2 in addition to being silica-rich. In igneous melts, Ti is a minor constituent, but can play a significant role in altering the structure of silicate melts and can affect the thermodynamic and physical properties of the melt (Cormier et al., 1998; Gan et al., 1996). For example, the viscous flow of silicate melts is, at least, partially dependent on the bond strength, which is altered by additional melt constituents (such as TiO_2) and their respective bond lengths and coordination; see (Le Losq et al., 2019) and (Richet and Mysen, 2019) for a review on the subject.

Due to the ability of Ti to act as both a glass modifier and former, relatively abundant presence in natural minerals and glasses, and its applications as a nucleating agent in glass-ceramics (Beall et al., 2012; Fernandes et al., 2013; Kajiwar, 1988; Krzmann et al., 2012), this study seeks to understand the glass structure of Ti-doped nepheline (NaAlSiO_4) glass, specifically, the local structure and role of Ti^{4+} within the glass matrix and its ability to substitute

for Si^{4+} in the glass network. Nepheline glass is considered to be a metaluminous composition (Mysen and Toplis, 2007), and Al in nepheline glass has been found previously to be four-fold coordinated acting as a network former (Lee and Stebbins, 2000; Marcial and McCloy, 2019). Addition of Al to the glass could make the silica network more flexible to promote the formation of $^{[4]}\text{Ti}$ as discussed, in addition to the presence of the glass modifier and charge compensator, Na. In this study, the glass structure is characterized through pair distribution function (PDF) analysis obtained from both X-ray and neutron total scattering experiments. To confirm the local environment of Ti within the glass, further characterization via Ti K-edge X-ray Absorption Spectroscopy (XAS) and Raman spectroscopy were performed

2.0 Experimental

2.1 Sample Preparation, Physical, and Chemical Characterization

Glasses were batched from reagent-grade TiO_2 (Sigma Aldrich, >99.8 %), SiO_2 (U.S. Silica), Al_2O_3 (Fisher, >99.0 %), and Na_2CO_3 (Fisher, >99.5 %) to obtain the final compositions shown in **Table 1** and were melted at 1650 °C in an electric furnace. Prior to melting, batch materials were mixed using an agate mortar and pestle to ensure a homogenous batch. All samples were melted in Pt-Rh crucibles for one hour and quenched by dipping the bottom of the crucible into a room temperature water bath. The resulting glasses were crushed using a tungsten-carbide (WC) ring mill for 0.06 minutes. The powdered glasses were then melted again for one hour; a second melt ensured a homogenous melt and glass. Nomenclature of the $\text{NaAlTi}_x\text{Si}_{1-x}\text{O}_4$ glasses is shown as x -Ti-NAS, x is the mole fraction substitution for Si. All compositions with Ti content up to and including 0.3Ti-NAS formed bulk glasses (**Table 1**). Glasses with a higher Ti content resulted in crystallization of TiO_2 on the glass surface upon quench. In the fully Ti-substituted glass, NAT, a bulk ceramic material was formed.

Helium pycnometry was performed with a Micromeritics Acupyc II 1340 gas pycnometer on pieces of glass with masses between 0.5-1.0 g in a 1.0 cm³ sample chamber that had been calibrated using the manufacturer's standard. Each sample was measured ten times and the results were averaged to obtain the final mass density (**Table 1**). Densities of all glass samples were also measured using the Archimedes method with toluene as the immersion liquid as it does not react with glasses, has a good wetting power, and has a well-known density including temperature dependence. Results are an average of measurements made on four distinct pieces of glass (**Table 1**).

Chemical compositions of the glasses have been measured using a Cameca SXFive electron microprobe (**Table 1**), with a 30 nA current, U=30 kV, and 5 s of counting. These chemical compositions are the mean of five individual measurements. Glasses were prepared in polymeric resin, polished, and metallized.

2.4 Total Scattering

A summary of the samples on which the total scattering experiments and atomistic simulations were performed are shown in **Table 2** for reference.

2.4.1 X-Ray Total Scattering

X-ray total scattering measurements were conducted at beamline 6-ID-D at the Advanced Photon Source, Argonne National Laboratory, Chicago, IL with a wavelength of 0.12355 Å. Measurements were performed on fine powdered glass samples packed in 0.0395" (1.02 mm) inner diameter, 0.0435" (1.105 mm) outer diameter polyimide capillaries and sealed with epoxy. Synchrotron X-ray total scattering experiments were performed on all glass samples except 0.3Ti-NAS. Concurrent with sample measurements, measurements of the detector without an X-ray beam and of an empty capillary were taken in order to accurately subtract the dark current,

the background attributed to the capillary, and air scattering. Cerianite (CeO_2 , NIST Standard) was run as a calibrant to determine sample-to-detector distance, the beam center, and the detector tilt using Fit2D software (Hammersley, 1997). The final output of Fit2D was the intensity as a function of 2θ , $I(2\theta)$.

GudrunX (Soper, 2011) software was used to process the reduced intensity data as a function of diffraction angle, $I(2\theta)$, to the total structure factor, $F(Q)$. GudrunX also performed the Fourier transform of the $F(Q)$ to obtain the Pair Distribution Function (PDF) normalized to single atom scattering, referred to as $g(r)$ in this work. For further definition of the functions used in this study, see (Keen, 2001; Marcial and McCloy, 2019). Densities utilized in GudrunX were determined via He-pycnometry, as described above. A Q -range of 0.04-18.0 \AA^{-1} with a step size of 0.04 \AA^{-1} was used as the range for useable data as well as for the final $F(Q)$. An r -max for the final $g(r)$ was set to be 17.0 \AA with a step size of 0.01 \AA . A Breit-Dirac factor was applied ranging from -5 to -9. A top-hat width (for the Lorch function) of 1.7 \AA was utilized and 1.25 \AA was used as the minimum radius for the Fourier transform. The sample ‘tweak factor’ (1/packing fraction) was set to 1.5 as the samples were powders and were likely not packed with 100% efficiency in the capillaries.

2.4.2 Neutron Total Scattering

Neutron total scattering experiments were conducted at the NOMAD (BL-1B) beamline at the Spallation Neutron Source of Oak Ridge National Laboratory. Measurements were performed on fine powdered glass samples packed in 3 mm (outer diameter), 0.1 mm thick fused quartz capillaries. Each sample was measured four times and summed to obtain the final $F(Q)$ with a Q -range of 0-31.4 \AA^{-1} . An empty vanadium can was used as the incoherent neutron scatterer, which was used to obtain the $F(Q)$. A diamond standard in a vanadium can was used to

determine the sample-to-detector bank distances implemented in converting the neutron time-of-flight to the magnitude of the momentum-transfer vector, or Q -space. A Fourier filter was applied to remove spurious peaks below 1.3 Å, below which no known atomic bonds are present for this system. For further information on this, the reader is referred elsewhere (Marcial and McCloy, 2019; Neuefeind et al., 2012).

2.4.3 Structure Modeling

Empirical Potential Structure Refinement shell (EPSR) was used to model the experimental $F(Q)$, obtained from neutron and X-ray total scattering experiments, via a co-refinement method where the X-ray and neutron $F(Q)$ are simultaneously fit (Soper, 2009). The co-refinement method was performed on NAS, 0.1Ti-NAS, and 0.2Ti-NAS. For 0.3Ti-NAS, only the neutron data was modeled using EPSR (X-ray scattering was not obtained). The modeled $F(Q)$ data was then Fourier transformed by EPSR to obtain the modeled $g(r)$ for comparison to the experimentally obtained $g(r)$ for both neutron and X-ray data; EPSR does not directly model $g(r)$. The reference potentials shown in **Table 3** and the atom box parameters shown in **Table 4** were defined prior to EPSR simulation. In the EPSR potentials, the parameters ϵ and σ control the depth and width of the potential energy well, while M is the atomic number and q the valence of the ion.

Prior to starting the simulation, all atoms were distributed randomly through the atom box. The temperature was then set to 10,000 K and simulations were allowed to run until the internal energy of the system had equilibrated. Once the internal energy had equilibrated, the temperature was dropped to 5,000 K, and then to 300 K. Once the internal energy had equilibrated at 300 K, the reference potentials were refined. Next, the total empirical potential of the system was sequentially increased to 50, 100, 150, 200, and 250, allowing for further

refinement of the reference potentials. A sequential increase of the empirical potential allowed for a refinement of the reference potentials as well as a systematic increase of the internal energy of the atom box, allowing for a best possible fit of the experimental data.

Average coordination numbers were calculated by EPSR by counting the number of nearest neighbors within a user-defined distance window (**Table 5**); distance windows were defined based upon the modeled individual $g(r)$'s. Average coordination numbers were additionally determined through visualization of the inflection point in the $N(r)$ curve, called the running coordination number, calculated by EPSR, with $N_{ij}(r)$ being defined as the number of atom type i surrounding atom type j located at radial distance, r (Marcial and McCloy, 2019). The function $N_{ij}(r)$ is an average, such that $N_{ij}(r)=4\pi\rho_A r^2 \times dg_{ij}(r)/dr$, where ρ_A is the atomic number density, which was calculated from densities determined through He-pycnometry in this study, and $g_{ij}(r)$ is the partial pair distribution function of components i and j scaled with either the neutron or X-ray scattering lengths. Not all neutron data sets were modeled due to low amounts of Ti in the glasses, resulting in relatively few Ti atoms in the atom box used for EPSR compared to the total atom count.

2.5 Ti K-edge X-ray Absorption Spectroscopy (XAS)

Ti K-edge X-ray absorption spectroscopy (XAS) was collected at two different synchrotron beamlines. Samples for XAS were dispersed in polyethylene glycol (PEG) with ratios optimized to achieve approximately one absorption length thickness while maintaining a suitable Ti K-edge absorption edge step.

2.5.1 KEK Light Source

Samples were measured in transmission mode on beam line BL-27B at the PF Ring of the Photon Factory synchrotron facility (Tsukuba, Japan), which operates at 2.5 GeV with a 300 mA

ring current. BL-27B uses a double crystal Si(111) monochromator with a sagittal focussing mechanism, and the energy range accessible extends from 4 to 20 keV. Beam size was restricted to 1 mm (H) and 3 mm (W) using slits and the intensity of the incident (I_0) and transmitted (I_t) X-ray intensities were measured using ionization chambers which could be filled with a variety of gases to tailor the absorption in each chamber (Konishi et al., 1996). Spectra were recorded between 4836 and 5700 eV with energy steps of 4 eV (4836 – 4956), 0.25 eV (4956 – 5000), 2 eV (5000 – 5250), and 4 eV (5250 – 5700). An accumulation time of 1 s step⁻¹ was used for all regions. For each sample, 3 to 30 spectra were averaged (depending on the Ti concentration) to improve the signal to noise ratio. To ensure accurate energy calibration, a transmission spectrum of a Ti foil was acquired and the position of the first inflection point in the derivative spectrum was set to 4966 eV (Bearden and Burr, 1967). The reference foil was also measured after each sample to check the monochromator energy calibration and provide energy reproducibility, between sets of scans, of ± 0.05 eV.

Spectra were recorded for five glasses (0.075Ti-, 0.1Ti-, 0.2Ti-, and 0.3Ti-NAS) and three crystalline standards. The crystalline standards used were: TiO₂ rutile (Sigma Aldrich) containing Ti⁴⁺ in octahedral coordination, the mineral fresnoite (Ba₂SiTi₂O₈) from Junnila Mine, California (BM.2000,121: sample kindly supplied by the British Natural History Museum) containing Ti⁴⁺ in five-fold coordination, and Ni_{2.6}Ti_{0.7}O₄ spinel synthesised from reagent grade precursors according to Lager et al. (Lager et al., 1981), which contains Ti⁴⁺ in tetrahedral coordination. All standards were confirmed to be phase pure by X-ray diffraction.

2.5.2 National Synchrotron Light Source-II

Samples were also measured at the National Synchrotron Light Source II (NSLS-II) at Brookhaven National Laboratory (Upton, New York), beamline 6-BM. Spectra of all six glasses

(0.025Ti-, 0.050-Ti, 0.075Ti-, 0.1Ti-, 0.2Ti-, and 0.3Ti-NAS) were collected in both fluorescence and transmission mode. 6-BM utilises a 3-pole wiggler source and delivers X-ray in the energy range between 4.5 and 23 keV. The optical system consists of a parabolic collimating mirror (5 nm Rh on 30 nm Pt), Si(111) and Si(311) monochromators, a toroidal focussing mirror, and a flat Pt-coated harmonic rejection mirror. Several modes of operation are possible on the beamline. For this study, the Si(111) monochromator and an unfocused beam was used; the beam was collimated to 0.5 mm in the vertical and 6 mm in the horizontal using slits. Ionization chambers were used to measure the incident and transmitted X-ray energies in transmission geometry and a SII Vortex ME4 (4-element Si drift) detector was used to simultaneously collect the fluorescence signal. The samples were mounted at 45° to both the incident X-ray beam and the vortex detector. The fluorescence signal was dead-time corrected a previously described (Woicik et al., 2010). Spectra were recorded between 4766 and 5606 eV with energy steps of 10 eV (4766 – 4936), 2 eV (4963 – 4956), 0.25 eV (4956 – 4996), and 0.5 eV (4996 – 5606). An accumulation time of 0.5 s step⁻¹ was used for the first three regions and 0.25 s step⁻¹ for the final region. For each sample, 6 to 12 spectra were averaged (depending on the Ti concentration) to improve the signal to noise ratio. To ensure accurate energy calibration, a transmission spectrum of a Ti foil reference was acquired simultaneously with each sample. The Ti foil was placed downstream of the sample between the transmission (I_t) and reference (I_r) ion chambers.

2.5.3 Data reduction

Data reduction and subsequent analysis was performed using the Demeter suite of programs (Athena, Artemis, and Hephaestus) (Ravel and Newville, 2005a, b), for X-ray Absorption Near Edge Structure (XANES) and Extended X-ray Absorption Fine Structure (EXAFS). Initial processing of the data sets involved using a standard background subtraction

and edge step normalisation procedure (Newville, 2001; Ravel and Newville, 2005b). The energy of the first maximum in the derivative of the energy spectrum for the Ti foil in the NSLS-II reference channel was calibrated to 4966.0 eV, and after normalization and energy alignment, direct comparisons between the Ti K-edge XANES for the samples could be made. Each Ti foil measurement made at KEK was aligned to the calibrated NSLS-II foil data and the same energy adjustment was then applied to the corresponding samples or standard. A cubic spline function was used to model the background; this was subtracted from the normalized data.

2.5.4 Pre-edge analysis

The pre-edge is related to electronic transitions occurring between the 1s and 3d energy levels and is a feature common to the K-edge spectra of many transition metals. Lower oxidation states have fewer unfilled 3d levels, so transitions from the 1s levels become less probable and the intensity of this feature becomes less well-defined; here all the Ti atoms are assumed to be Ti^{4+} , and only these standards were considered. The normalized height of the pre-edge also decreases significantly as a result of an increase in centro-symmetry (i.e., the pre-edge is less distinct for octahedral than tetrahedral symmetry) (Yamamoto, 2008).

It has been shown for many transition metals, including Ti, that the fitting of the pre-edge to the white line can give information about valence and coordination number in glasses (Chalmin et al., 2009; Farges et al., 1996a; Farges et al., 2005). The glasses and the three standards were measured and a fitting routine was applied to analyze the pre-edge features. The standards included representative $[\text{6}]\text{Ti}^{4+}$ (rutile, TiO_2), $[\text{5}]\text{Ti}^{4+}$ (fresnoite, $\text{Ba}_2\text{TiSi}_2\text{O}_8$), and $[\text{4}]\text{Ti}^{4+}$ (spinel, $\text{Ni}_{2.6}\text{Ti}_{0.7}\text{O}_4$). For the pre-edge analysis, a series of Gaussians was fit in the 4960 – 5040 eV range, and the contribution for the pre-edge was extracted (Farges et al., 1996c). From

this, the centroid and normalized height were determined, with the energies and heights being distinctive for coordination environments of Ti^{4+} .

2.5.5 EXAFS analysis

Subsequently, energy values in eV were converted to k (\AA^{-1}) to give the k^3 weighted $\chi(k)$ data. Applying a Fourier transform (FT) to the data yielded a partial radial distribution function (RDF) where peaks represent shells of atoms surrounding the central Ti absorber atom. For each shell of atoms, the path length (R), the thermal parameter (σ^2), and the coordination number (N) were extracted by fitting the data to a suitable starting model.

The local structure around the Ti scatterer was obtained from the XAS by fitting the EXAFS using Artemis software (Ravel and Newville, 2005a, b). The data from KEK was used for the fitting. Determination of the local structure in the glass samples requires an independent determination of the amplitude reduction factor (S_0^2) term in the EXAFS equation (Kelly et al., 2008). First, the amplitude reduction factor S_0^2 ($= 0.65 \pm 0.03$) was obtained by fitting the TiO_2 (rutile) standard using the structure from a crystallographic information file (Baur and Khan, 1971), and computing the scattering paths using FEFF. This refined amplitude reduction factor was then used to fit the glasses 3Ti-NAS, 2Ti-NAS, 1-Ti-NAS, and 075Ti-NAS.

The first coordination shell of oxygen was modeled using a Ti-O scattering path generated using FEFF and the structural model given in the crystallographic information file (CIF) for $\text{NaTi}_2\text{Al}_5\text{O}_{12}$ (Mumme and Wadsley, 1967). The oxygen coordination number around the Ti ($N_{\text{Ti-O}}$), the change in the Ti-O bond length ($\delta R_{\text{Ti-O}}$), the Debye-Waller thermal factors for oxygen (σ_{O}^2), and the change in the absorption edge energy (δE_0) were all allowed to refine. This approach returned a satisfactory fit to the intense feature in the low radial distance range of the FT $k^3\chi(k)$. In order to fit the spectral features at higher radial distance, three additional scattering

paths were added. Two scattering paths, Ti-Al and Ti-Ti, were taken from the $\text{NaTi}_2\text{Al}_5\text{O}_{12}$ model and the third path (Ti-Si) was generated from the $\text{Na}_2\text{TiSiO}_5$ CIF (Ziadi et al., 1996). The coordination number was kept fixed at two for these additional contributions. An attempt was made to include a Ti-Na scattering path, but this did not yield an improvement in the fit. For each additional scatterer, $\delta R_{\text{Ti-i}}$ (where $R_{\text{Ti-i}}$ indicates the average interatomic distance for a given Ti-i pair) and σ_i^2 were refined simultaneously.

2.6 Raman Spectroscopy

Raman spectra were collected on a Jobin-Yvon Horiba T64000 Triple-spectrometer with confocal system through an Olympus BX40 microscope. Samples were excited using a 488.1 nm Coherent Genesis MX SLM laser running at 500 mW output power. The detector was a liquid nitrogen cooled CCD camera. The spectrometer was calibrated using the 520.7 cm^{-1} line of single crystal Si to within 0.6 cm^{-1} . Spectra were collected through a 100x objective, from 25 to 1300 cm^{-1} , for count times of 200 s, with three subsequent spectra averaged.

3.0 Results

3.1 Glass density and chemistry

All single-phase glasses prepared in this study were analyzed via EPMA and their densities were measured using the Archimedeian method with toluene as an immersion liquid and He pycnometry. Results are shown in **Table 1** and compared with the theoretical as-batched compositions.

3.2 Pair Distribution Function Analysis

Pair distribution function (PDF) analysis was performed on the samples listed in **Table 2**. Neutron total scattering data is shown in **Figure 1**. EPSR simulation fits of both neutron and X-

ray obtained $F(Q)$, and the resulting $g(r)$, are shown in **Figure 2**. The deconvoluted $g(r)$ functions were calculated from the EPSR atom model and are shown in **Figure 3**. These deconvoluted $g_{ij}(r)$ functions result in the first peak being a combination of Si-O, Ti-O and Al-O pair correlations, with the Si-O correlations being at a slightly shorter distance than that of Ti-O and Al-O. The Ti-O and Al-O bond lengths are nearly identical in these glasses, but this overlap is not problematic due to the negative scattering length of natural Ti in neutron total scattering experiments (see **Table A-1** and discussion in Appendix). By comparing X-ray and neutron total scattering experiments in an EPSR co-refinement, the Ti local environment can be distinguished from that of Si and Al local environments. Na-O does not contribute to the first peak in the $g_{Na-O}(r)$, but rather in the second peak, occurring around 2.5 Å.

Through observation of the deconvoluted $g_{ij}(r)$, or partial PDF, bond distance windows were defined and used to calculate the coordination numbers. The resultant calculated coordination numbers are shown in **Table 5**. As a secondary means to determine the coordination numbers of species within the glasses, $N_{ij}(r)$ functions were calculated and plotted, the results are shown in **Figure 3**. The $N_{ij}(r)$ functions are independent of user-defined distance windows; rather, they are derived directly from the partial PDF's by EPSR.

Looking specifically at the EPSR calculated coordination numbers (**Table 5**), the Si-O coordination and Al-O coordination remained approximately four, regardless of the Ti addition to the glass. The Na-O coordination number calculations did not result in one consistent coordination number for Na. The coordination of Na in NAS (nepheline) glass was approximately six. The Na-O coordination increased in the 0.1Ti and 0.2Ti glasses with a coordination number of 6.23 and 6.50, respectively. In the 0.3Ti glass, the Na-O average coordination decreased below six for an average coordination of 5.46. Coordination numbers

determined via this method are dependent upon the user definition of a bond-distance window; too large of a window can result in including atoms that are not directly bonded to the species of interest within the calculation, while too small of a distance window results in excluding atoms of interest.

Comparing these coordination numbers to those shown in the $N_{ij}(r)$ plots, Si, Al, and Ti all have coordination numbers approximately of four, with Ti having a slightly higher average coordination. An average Ti-O coordination number larger than four could indicate a minor contribution of $^{[5]}\text{Ti}$ or $^{[6]}\text{Ti}$ (with the majority of atoms present as $^{[4]}\text{Ti}$). Looking at the atom model from EPSR, Ti is primarily four-fold coordinated, but in the case of the 0.1Ti atom model, a small amount of $^{[5]}\text{Ti}$ was observed, see **Figure 4A**. The coordination of Na-O in the $N(r)$ plots is not as well defined, because the inflection point, which is used to determine the coordination number in these functions, is not as clear and does not plateau in the same way that Si-O, Al-O, and Ti-O do in their respective $N(r)$ plots.

Further inspection of the atom models exported from EPSR (**Figure 4**) shows $^{[4]}\text{Ti}$ tetrahedra linking with $^{[4]}\text{Al}$, $^{[4]}\text{Si}$, and in some cases other Ti polyhedra through bridging oxygen bonds. These atom models show Na atoms interspersed throughout the network of Al, Si, and Ti. In addition to using EPSR to determine bond distances and coordination numbers, the exported atom models were visualized using CrystalMaker (Oxfordshire, UK), using defined bonding distance windows also used in EPSR. The resulting coordination numbers are shown in **Table 5**. Atom distributions around Ti for the exported atom model are shown in **Figure 4**; here the first coordination sphere is shown to consist of oxygen atoms, as indicated by the first peak. The second coordination sphere is an overlap of Al, Ti, and Si contributions.

3.3 Ti K-edge XAS

The normalized Ti K-edge XANES spectra for all the glass samples are offset and compared to mineral standards in **Figure 5**. The XANES region contains qualitative information about the mid-range ordering around the Ti atoms in the glass and the trends observed here suggest there is increased ordering around the Ti atoms with increasing Ti concentration (Farges et al., 1996c; Farges et al., 1997).

Visual inspection of the pre-edge region in the stack plot (**Figure 5a**) indicates that the Ti atoms in the glass are in a similar tetrahedral coordination environment to those in the spinel structured $\text{Ni}_{2.6}\text{Ti}_{0.7}\text{O}_4$. The centroid energy and peak heights calculated for the standards and the glasses were compared against published results in the literature (Farges et al., 1996c). This comparison is shown in **Figure 6**, and the standards all sit within the expected regions on the plot which are defined in terms of the local Ti environment.

The position of the centroid energy and the peak height suggest that Ti is in a tetrahedral environment in all glasses. This is consistent, within error, with the EXAFS fitting described below. To ensure consistency in the pre-edge analysis, average values for the centroid energy position and the peak height were calculated from the fluorescence and transmission data collected at NSLS-II. Independent fitting of the KEK glass data yield results slightly different, but within the tetrahedral domain. It should be noted that differences in beamline alignment and calibration, and the normalization and fitting procedure used (i.e., fitting Gaussians to the whole XANES spectral envelope versus fitting only the pre-edge feature) can affect the final position on the plot. Nonetheless, the results consistently suggest overwhelming dominance of $^{[4]}\text{Ti}^{4+}$.

The EXAFS fits are shown in **Figure 7** and the refined model parameters are given in **Table 6**. To validate the refined path lengths, the bond valance sum (BVS) approach was used

(Brown and Altermatt, 1985). The bond valence was calculated using an observed bond length (r_0') of 1.815 Å and empirical constant (B) of 0.37. The BVS was then calculated by multiplying this value by the number of coordinated oxygens refined in the EXAFS fit. Obtained BVS's were between 3.50 and 3.75, with typical errors of 0.5 – 1.0 valence unit (v. u.), reasonably close to the expected 4.0 for Ti^{4+} .

From the final EXAFS structural parameters, it can be observed that the local structure of the glasses changes between 0.1Ti-NAS and 0.2Ti-NAS. For the lower Ti concentrations (0.075Ti and 0.1Ti), the second nearest neighbor (2NN) to the Ti scatterer is another Ti atom, ~2.46 Å, implying Ti clustering behavior. Additional neighboring Al and Si distances were refined at ~3.00 Å and ~3.25 Å, respectively. For the larger Ti concentrations (0.2Ti and 0.3Ti), the 2NN for the Ti scatterer is Al at 2.76 Å; a third shell containing Si atoms and Ti in the same coordination sphere (within errors) was refined at ~3.00 Å. This change in local structure qualitatively agrees with the change in the XANES region (see **Figure 5b**) which shows increased structure for 0.3Ti and 0.2Ti, while the glasses with lower Ti appear to overlay each other in that region.

3.4 Raman Spectroscopy

Raman spectra are shown in **Figure 8**. The spectra are composed of several bands. A broad band is observed at ~80 cm^{-1} , followed by a small peak located at ~290 cm^{-1} . An intense peak is present at ~490 cm^{-1} , with a small shoulder near 560 cm^{-1} . A large and not very intense peak is observed at ~730 cm^{-1} . A broad band is observed near ~1000 cm^{-1} , and Ti-bearing glasses also show an intense band at 890 cm^{-1} .

Increasing the Ti content in the glass results in several clear changes in those signals. First, peaks present in the NAS glass spectrum generally become broader and less defined with

Ti addition. The other two noticeable changes with Ti addition are (i) the band at $\sim 290\text{ cm}^{-1}$ becomes more intense and better defined, and (ii) a peak at $\sim 890\text{ cm}^{-1}$ appears and increases in intensity at the expense of the $\sim 1000\text{ cm}^{-1}$ peak originally present in the NAS glass. The relative intensity of the two 890 cm^{-1} and $\sim 1000\text{ cm}^{-1}$ bands is represented as a function of the Ti/(Ti+Si) ratio of the glasses in **Figure 9**. The evolution of this relative intensity as a function of the Ti/(Ti+Si) ratio is not linear and shows a logarithmic trend. This indicates that the Raman cross section of the vibration giving the signal near $\sim 890\text{ cm}^{-1}$ is very different to that of the vibrations giving the $\sim 1000\text{ cm}^{-1}$ signal in the NAS glass, and that the signal mixture between those two different vibrations is a non-linear process.

4.0 Discussion

4.1 Short Range Ordering through PDF analysis

This study focuses on understanding the compositional influence of the glass structure after quenching. Through the PDF analysis, it can be concluded that Si and Al are four-coordinated and act as network formers, regardless of the Ti content of the glass; there is no observable change in the Al-O and Si-O bond distance. This has been previously determined for other nepheline-based glass compositions by using similar methodology (Marcial and McCloy, 2019).

The local environment of Na is less ordered, compared to Si and Al, and varies with the Ti content of the glass. The average coordination of Na in NAS (nepheline) glass was approximately six, which is in agreement with (Marcial and McCloy, 2019), where EPSR was also utilized in calculating coordination numbers. In another study on nepheline glass, Na was observed by XANES at the Na K-edge to be nine-fold coordinated (Neuville et al., 2004). Differences in the Na coordination number could be due to the experimental difference, total

scattering is a technique looking at the average structure of the material, whereas, XANES is atom specific. Calculations in Na coordination number could also have variation due to the relatively disordered local environment of Na because of its role as a network modifier or charge compensator. As the Ti content increased, the Na coordination was observed to also increase, until the 0.3Ti sample, in which the Na coordination was at its lowest observed value for this study, as observed from EPSR calculations for a user-defined distance window.

Comparing this to the $N(r)$ plot for Na-O correlations, the inflection point is not well defined, which indicates that there is not one defined coordination number. The lack of definition of the $N_{Na-O}(r)$ function could be attributed to two things, (i) Na has a relatively small X-ray cross-section compared with the other species within the glass, and (ii) the Na-O local environment may not be as well defined as a SiO_4 tetrahedron; for example, there could be a variety of bond lengths and coordination associated with Na-O due to a high degree of disorder around the Na atoms. Marcial and McCloy (Marcial and McCloy, 2019) found that Na, Li, and Ca in aluminosilicate glasses varied considerably in coordination numbers, all of which are modifier species. In the case of Na, it was found that the Na-O coordination number as determined by PDF ranges from two to ten, with the majority being between five- and seven-coordinated, and an average of six-fold coordinated (Marcial and McCloy, 2019).

Comparing the coordination numbers calculated by EPSR discussed previously, and the coordination numbers calculated through CrystalMaker, there is some discrepancy in the values. Specifically, the coordination numbers observed through CrystalMaker are consistently lower than those calculated via EPSR and those observed in the $N(r)$ plots (**Figure 3**). This is due to the fact that EPSR averages the final result over a series of ensembles (configurations), to give an averaged overall coordination number. By contrast, when the atom model is exported to

CrystalMaker, the model is only representative of one configuration of the EPSR model. There is value, though, in looking at the CrystalMaker results, as the second coordination sphere can be visualized, as shown in **Figure 4**.

Overall, when taking all methods of PDF analysis represented here, the local structure around Si, Al, and Na does not drastically change in terms of coordination numbers and bond distances. Further insight into the overall glass structure is provided through Raman spectroscopy.

4.2 Structure Implications through Raman spectroscopy

Three domains of interest can be considered in **Figure 8**. The first one is the Boson region ($< 200 \text{ cm}^{-1}$), where the Boson peak is visible at a Raman shift of $\sim 70 \text{ cm}^{-1}$. Its origin remains controversial but related to vibrations and librations of network-forming polyhedral units (Buchenau et al., 1986; Greaves et al., 2005; Hehlen et al., 2002), such that it is sensitive to changes at medium range order. The second region is located in the range $200\text{-}800 \text{ cm}^{-1}$. In this portion of Raman spectra, inter-tetrahedral vibrations of T-O-T (with T a network forming cation like Si) are observed, and for the present compensated glasses they are built from vibrations of rings of tetrahedral units (Galeener, 1982; McMillan, 1984; Sharma et al., 1985). Finally, the last region of interest is located between 800 and 1300 cm^{-1} . In aluminosilicate glasses, bands in this domain can be assigned to T-O stretching vibrations in the polyhedral units building the network framework (McMillan, 1984; Mysen et al., 1982; Virgo et al., 1980). In Ti-bearing glasses, the $\sim 890 \text{ cm}^{-1}$ peak is assigned to Ti-O vibrations in the glass network (Mysen and Neuville, 1995).

When Ti substitutes for Si, the $\sim 890 \text{ cm}^{-1}$ peak assigned to Ti-O vibrations increases in intensity as expected. The mixture between the two Ti-O and (Si,Al)-O stretching signals is non-linear (**Figure 8**), rendering any attempts to decompose the signals as a linear mixture of two

signals futile. More information actually is embedded in the increase of the signal near ~ 290 cm^{-1} . This band may be assigned to a signal from the alkali metal charge compensator cation in its cage, similarly to what has been previously proposed for network modifier cations (Hehlen and Neuville, 2015). The increase of a similar peak is observed with substitution of Na by K in tectosilicate glasses (Le Losq and Neuville, 2017), a phenomenon accompanied by increasing segregations of alkalis in compensator channels, following the Charge Compensated Random Network (CCRN) model (Greaves and Ngai, 1995). Accordingly, the present observations (**Figure 8**) may indicate that, in the presence of Ti, the Na environment tends to become more organized, with the appearance of more clusters and channels of Na compensator cations in the glass structure. Considering that nodes of non-network former cationic channels are preferential nucleating locations (Dargaud et al., 2012), such organization and segregation of Na may help explaining the fact that TiO_2 is a nucleating agent in aluminosilicate glasses. This will be further promoted by a reorganization of the Na environment in glasses before crystallization, as has already been supported by XANES studies. This is also consistent with the fact that when the TiO_2 is increased beyond 15 mol%, the glasses of corresponding composition could not be synthesized due to crystallization upon quench.

4.3 Coordination and glass-forming role of Ti

Based on the PDF analysis, it was determined that Ti is primarily $^{[4]}\text{Ti}$ in the nepheline glass series where Ti is substituted for Si, with $^{[5]}\text{Ti}$ or $^{[6]}\text{Ti}$ being present in only minor amounts. There is a general lack of data concerning Ti-containing aluminosilicate glasses in literature, but in one study, the local structure of Ti was determined by XANES as the Al content in the glass was increased (Romano et al., 2000). It was found that the addition of Al promotes the formation of $^{[4]}\text{Ti}$ through destabilization of $^{[5]}\text{Ti}$ pyramids, as the alkali cations are used to charge

compensate the Al^{3+} in $^{[4]}\text{Al}$ tetrahedra (Romano et al., 2000). According to the initial PDF analysis conducted here, Al is four-fold coordinated in all glasses, which requires charge balancing cations, such as Na. This could indicate that there is a majority of $^{[4]}\text{Ti}$ from the standpoint of Ti content (Henderson and St-Amour, 2004) and presence of Al (Romano et al., 2000).

With stoichiometric nepheline glass, NaAlSiO_4 , the network is theoretically fully polymerized and charge net-neutral, meaning every $^{[4]}\text{Al}$ tetrahedron and $^{[4]}\text{Si}$ tetrahedron has four bridging oxygen and every $^{[4]}\text{Al}$ tetrahedron is charge compensated by one Na atom. If Ti is five-fold coordinated within the glass network, Na would be required for charge compensation, and would be in competition with four-coordinated Al, as stated in (Romano et al., 2000). If Ti were to be four-coordinated, it would have a neutral charge, and there would be no competition for Na cations between Ti and Al for charge compensation. Through the Al-O coordination number calculations via EPSR, Al has a consistent average coordination of four and does not vary with Ti addition. Because there is not an excess of Na, or other charge compensating cations, five-fold coordinated Ti is likely unfavorable. From this standpoint, the average EPSR calculated Ti-O coordination of four, or slightly higher than four, is reasonable.

The XAS data support this interpretation. The pre-edge height and energy, as well as the bond length, are consistent with $^{[4]}\text{Ti}$ (Farges et al., 1996c). The average pre-edge for all the glasses is similar to the pre-edge in the $\text{Ni}_{2.62}\text{Ti}_{0.7}\text{O}_4$ spinel standard. The XANES region, containing information about the mid-range ordering in the glass around Ti (Farges et al., 1996c; Farges et al., 1997), shows trends suggesting increased ordering with increased Ti concentration, which is consistent with the interpretation of the Raman spectra. It is likely that the second-nearest-neighbors after oxygen in the Ti shell are Na atoms in disordered positions, based on

previous modeling of Ti K-edge spectra of silicate glasses (Farges et al., 1996a), at least for the high Ti glasses here. It has also been found in $\text{TiO}_2\text{-Al}_2\text{O}_3\text{-SiO}_2$ glasses that, when Ti substitutes into the glass network as a former, it has a stronger affinity for Al than for Si due to AlO_4^- requiring charge compensation (Kirschen et al., 1999). In the glasses here, since the Na atoms are used to charge compensate the AlO_4^- units, the local structure then involves ^{47}Ti connected to AlO_4 tetrahedra with interspersed Na atoms, indicating an increase of Ti-O-Al bonding as Ti is substituted for Si. Differences observed in coordination number between the PDF analysis and XAS can be attributed to the fact that the X-ray and neutron total scattering, and subsequent PDF, do not probe one specific atom, but rather look at the glass as a whole, whereas XAS looks specifically at the Ti local environment.

The influence of Ti on glass formability is compositionally dependent. For the case of $\text{NaAl}(\text{Si},\text{Ti})\text{O}_4$ glasses studied here, when subjected to traditional melt-quenching, the glass formation region was found to extend to $\text{NaAlTi}_{0.3}\text{Si}_{0.7}\text{O}_4$. Through PDF analysis, XAS, and Raman spectroscopy, it is believed that for the currently considered $\text{NaAl}(\text{Si},\text{Ti})\text{O}_4$ system, Ti tends to tetrahedrally coordinate with oxygen and substitutes Si in the lattice; therefore acting as a network former. Through the analysis of EXAFS data, a shift in the second coordination sphere of Ti was observed as the fraction of Ti increased. This could have implications for the crystallization behavior of these systems in the molten state, in addition to the reorganization of the Na environment as suggested by Raman spectroscopy observations.

Considering that these systems feature $\text{Al}/(\text{Si}+\text{Ti}) = 1$, in order to maximize the separation of positively charged AlO_4 tetrahedra, Ti would need to substitute directly for Si in the alternating Al-O-Si glass network. The observed tendency for Al to serve as the second

nearest-neighbor in glasses with higher Ti/Si ratios is consistent with Loewenstein's Al-avoidance rule (Loewenstein, 1954).

5.0 Conclusion

This work sought to identify the effect of TiO_2 on the structure of nepheline glass (NaAlSiO_4) via a systematic substitution for SiO_2 . Through neutron and X-ray total scattering experiments paired with EPSR atomistic simulations, Raman spectroscopy, and Ti K-edge XAS, the local environments within the glass were determined. Overall, it has been found that the Al and Si local environments, i.e. coordination numbers, remained constant as TiO_2 was introduced into the glass. Na coordination showed a non-linear variation in coordination as TiO_2 content was increased, with an abrupt change between the $\text{NaAlTi}_{0.2}\text{Si}_{0.8}\text{O}_4$ (0.2Ti-NAS) and $\text{NaAlTi}_{0.3}\text{Si}_{0.7}\text{O}_4$ (0.3Ti-NAS) glasses, with additional changes in the Na environment being observed through Raman spectroscopy. Ti was found, via analysis to of the total scattering data, to be coordinated with, on average, approximately four oxygen atoms. XAS shows essentially four-fold coordinated Ti. There is no definitive indication of six-fold coordinated Ti from any of the techniques utilized in this study, but EPSR simulation may indicate a small contribution of five-fold coordinated Ti. Overall, up to 15 mol% (16 wt%) TiO_2 can be substituted for SiO_2 in NaAlSiO_4 while still maintaining a single-phase glass.

Acknowledgements

Funding for this project was provided through the by the United States Department of Energy (US DOE) Waste Treatment & Immobilization Plant (WTP) Federal Project Office under the direction of Dr. Albert A. Kruger, contract number 89304017CEM000001. A portion of this research used resources at the Spallation Neutron Source (SNS), a US DOE Office of Science

(OS) user facility operated by the Oak Ridge National Laboratory (ORNL); neutron scattering work was granted under ORNL SNS IPTS-21702.1. A portion of this research used resources of the Advanced Photon Source (APS), a US DOE OS user facility operated for the DOE OS by Argonne National Laboratory (ANL) under contract DE-AC02-06CH11357; the authors thank Dr. Xiaofeng Guo for use of his beamtime at the APS, Beamline 6-ID-D. A portion of this research used 6-BM of the National Synchrotron Light Source II (NSLSII), user proposal 301027, a US DOE OS user facility operated for the DOE OS by Brookhaven National Laboratory (BNL) under contract DE-SC0012704. A portion of this research used resources of the Photon Factory Advisory Committee, with beamtime at the High Energy Accelerator Research Organization (Kō Enerugī Kasokuki Kenkyū Kikō or KEK) facility in Tsukuba, Japan; the support of Yoshihiro Okamoto (Japan Atomic Energy Agency) during the experiment is gratefully acknowledged. This work was, in part, performed in the HADES/MIDAS facility at the University of Sheffield, established with financial support of the University of Sheffield, Department of Business, Energy and Industrial Strategy, and the Engineering and Physical Sciences Research Council under grant EP/T011424/1. JSM also gratefully acknowledges support from the US-UK Fulbright Commission for support during his sabbatical at the University of Sheffield. Parts of this work were supported by IPGP multidisciplinary program PARI, and by Region île-de-France SESAME Grant no. 12015908.

Appendix

A. X-ray Total Scattering using Lab-Scale X-ray Diffractometer

X-ray total scattering measurements were also performed on a Panalytical X'pert Pro Powder X-ray Diffractometer equipped with a Ag-K α source at 60 keV and 36 mA and a scintillator detector. Samples were packed in glass capillaries with 1.0 mm O.D. and flame sealed. Data was collected over 25 hours using a Variable Counting Time (VCT) program. Each sample, including an empty capillary, were run using the VCT program to obtain the X-ray total scattering data. Scans were conducted from 2-120° 2 θ with a step size of 0.06° 2 θ . From 2-40° 2 θ , one scan was performed, from 38-70° 2 θ , 5 scans were performed and summed, and from 68-120° 2 θ , 10 scans were performed and summed. VCT scan data were converted from total intensity to counts per second (cps) and stitched together using Highscore Plus software. A Bremsstrahlung file, which is X-ray source and instrument specific, was also obtained using a Si-311 single crystal wafer measured using an omega-theta scan. Using GudrunX, the background (attributed to air and container scattering) and the Bremsstrahlung contributions were subtracted, and the Fourier transform was carried out to obtain the $g(r)$, the pair distribution function, discussed previously in the experimental section of this work. The resulting $F(Q)$ and $g(r)$ obtained from the lab-scale XRD measurements are shown in **Figure A1**.

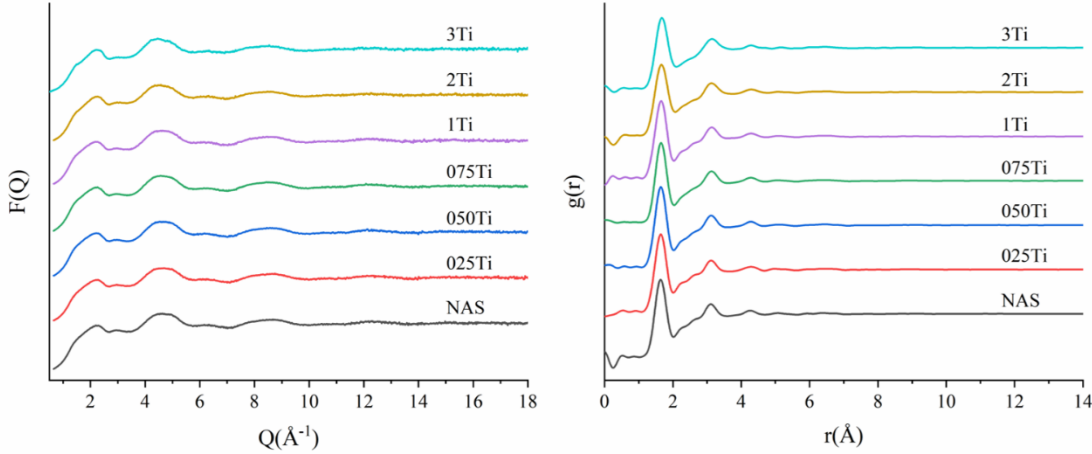


Figure A1- F(Q) and g(r) obtained through measurements on a lab-scale XRD equipped with a Ag source.

B. Neutron vs. X-ray Total Scattering Experiments

Neutron and X-ray total scattering experiments are complimentary techniques in the way that X-rays and neutrons are able to interrogate different atomic species within the glasses of this study based upon their scattering coefficient, b , and their X-ray cross section, see **Table B1**.

A scattering cross-section relates the probability of a scattering event from a sample (sample dependent) to the number of counts or signal reaching a detector (Darling, 2009). The scattering cross section for neutrons is represented by $\sigma_{\text{tot}} = 4\pi b^2$ where b is the atomic scattering length (Darling, 2009). Neutrons interact with the atom's nuclei with the scale of the interaction being dependent on the isotope and does not scale with Z . X-rays interact with the electron cloud instead of the nuclei. This results in a Z -dependence with the X-ray cross section. In this way, X-rays and neutrons can be complementary techniques as neutrons can distinguish between similar Z -elements as distinguish between different isotopes within a sample.

In the Ti-containing sodium aluminosilicate glasses in this study, neutron and X-ray total scattering allowed for determination of Ti partial PDF's and Si partial PDF's where the use of just X-ray total scattering would have been a limitation. The first peak in the $g(r)$ encompasses

Si-O, Ti-O, and Al-O partial PDF's with little peak resolution. To deconvolute this peak into the partial $g(r)$ functions, neutron scattering was paired with X-ray scattering. X-ray total scattering resulted in a net positive signal, while neutron total scattering resulted in a positive signal for Si, Al, and O contributions, but a negative signal for Ti contributions as Ti is a negative neutron scatterer. It is important to note that all samples were of natural isotopic abundance and the scattering coefficients were calculated as such for analysis and EPSR simulation.

Table B1-Neutron scattering length of atomic species within Ti-NAS glasses used in this study. All materials were of natural isotopic abundance. Scattering coefficients were obtained from (Sears, 1992).

Atomic Species	Coherent Scattering Length, b (fm)
Na	3.63
Al	3.449
Si	4.1491
Ti	-3.438
O	5.803

Research Data

Research Data associated with this article can be access at <http://dx.doi.org/10.17632/h85yj23ww4.1>

647 References

- 648 Alderman, O., Skinner, L., Benmore, C., Tamalonis, A., Weber, J. (2014) Structure of molten
649 titanium dioxide. *Phys. Rev. B* **90**, 094204.
- 650 Baur, W.H., Khan, A.A. (1971) Rutile-type compounds. IV. SiO₂, GeO₂ and a comparison with
651 other rutile-type structures. *Acta Cryst. B* **27**, 2133-2139.
- 652 Beall, G.H., American Ceramic, S., Höland, W. (2012) *Glass-ceramic technology*, 2nd ed. ed.
653 American Ceramic Society, Hoboken, N.J.
- 654 Bearden, J.A., Burr, A.F. (1967) Reevaluation of X-ray Atomic Energy Levels. *Rev. Mod. Phys*
655 **39**, 125-142.
- 656 Bernasconi, A., Dapiaggi, M., Bowron, D., Ceola, S., Maurina, S. (2016) Aluminosilicate-based
657 glasses structural investigation by high-energy X-ray diffraction. *J. Mater. Sci.* **51**, 8845–
658 8860.
- 659 Bernasconi, A., Dapiaggi, M., Pavese, A., Bowron, D., Imberti, S. (2012) Local Structure of Si-
660 Al-Ca-Na-O Glasses from Coupled Neutron and X-ray Total Scattering Data. *J. Phys.*
661 *Chem. B* **116**, 13114-13123.
- 662 Brown, I.D., Altermatt, D. (1985) Bond-valence parameters obtained from a systematic analysis
663 of the Inorganic Crystal Structure Database. *Acta Cryst. B* **41**, 244-247.
- 664 Buchenau, U., Prager, M., Nücker, N., Dianoux, A.J., Ahmad, N., Phillips, W.A. (1986) Low-
665 frequency modes in vitreous silica. *Phys. Rev. B* **34**, 5665-5673.
- 666 Chalmin, E., Farges, F., Brown, G.E. (2009) A pre-edge analysis of Mn K-edge XANES spectra
667 to help determine the speciation of manganese in minerals and glasses. *Contrib. Mineral.*
668 *Petrol.* **157**, 111-126.
- 669 Cicconi, M.R., Neuville, D. (2019) Natural Glasses, in: Musgraves, J.D., Hu, J., Calvez, L.
670 (Eds.), *Springer Handbook of Glass*. Springer, pp. 771-812.
- 671 Cormier, L., Gaskell, P., Calas, G., Soper, A. (1998) Medium-range order around titanium in a
672 silicate glass studied by neutron diffraction with isotropic substitution. *Phys. Rev. B* **58**,
673 11322-11330.
- 674 Dargaud, O., Cormier, L., Menguy, N., Patriarche, G. (2012) Multi-scale structuration of glasses:
675 Observations of phase separation and nanoscale heterogeneities in glasses by Z-contrast
676 scanning electron transmission microscopy. *J. Non-Cryst. Solids* **358**, 1257-1262.
- 677 Darling, T.W. (2009) Neutron Scattering in Earth Sciences. *Am. Mineral.* **94**, 1502-1502.
- 678 Farges, F., Brown, G.E., Navrotsky, A., Gan, H., Rehr, J.J. (1996a) Coordination chemistry of
679 Ti(IV) in silicate glasses and melts: II. Glasses at ambient temperature and pressure.
680 *Geochim. Cosmochim. Acta* **60**, 3039-3053.
- 681 Farges, F., Brown, G.E., Navrotsky, A., Gan, H., Rehr, J.R. (1996b) Coordination chemistry of
682 Ti(IV) in silicate glasses and melts: III. Glasses and melts from ambient to high
683 temperatures. *Geochim. Cosmochim. Acta* **60**, 3055-3065.

684 Farges, F., Brown, G.E., Rehr, J.J. (1996c) Coordination chemistry of Ti(IV) in silicate glasses
685 and melts: I. XAFS study of titanium coordination in oxide model compounds. *Geochim.*
686 *Cosmochim. Acta* **60**, 3023-3038.

687 Farges, F., Brown, G.E., Rehr, J.J. (1997) Ti K-edge XANES studies of Ti coordination and
688 disorder in oxide compounds: Comparison between theory and experiment. *Phys. Rev. B*
689 **56**, 1809-1819.

690 Farges, F., Rossano, S., Lefrère, Y., Wilke, M., G. E. Brown, J. (2005) Iron in silicate glasses: a
691 systematic analysis of pre-edge, XANES and EXAFS features. *Physica Scripta* **2005**,
692 957-959.

693 Fernandes, H., Tulyaganov, D., Ferreira, J. (2013) The role of P₂O₅, TiO₂ and ZrO₂ as nucleating
694 agents on microstructure and crystallization behaviour of lithium disilicate-based glass. *J.*
695 *Mater. Sci.* **48**, 765-773.

696 Fu, J. (2011) Photocatalytic properties of TiO₂-P₂O₅ glass ceramics. *Mater. Res. Bull.* **46**, 2523-
697 2526.

698 Galeener, F.L. (1982) Planar rings in glasses. *Solid State Comm.* **44**, 1037-1040.

699 Gan, H., Wilding, M.C., Navrotsky, A. (1996) Ti⁴⁺ in silicate melts: Energetics from high-
700 temperature calorimetric studies and implications for melt structure. *Geochim.*
701 *Cosmochim. Acta* **60**, 4123-4131.

702 Greaves, G., Meneau, F., Majerus, O., Jones, D., Taylor, J. (2005) Identifying Vibrations That
703 Destabilize Crystals and Characterize the Glassy State. *Science* **308**, 1299-1302.

704 Greaves, G.N., Ngai, K.L. (1995) Relating the atomic structure of aluminosilicate glasses to
705 their ionic transport properties. *J. Non-Cryst. Solids* **192-193**, 405-410.

706 Gregor, R.B., Lytle, F.W., Sandstrom, D.R., Wong, J., Schultz, P. (1983) Investigation of TiO₂-
707 SiO₂ glasses by X-ray absorption spectroscopy. *J. Non-Cryst. Solids* **55**, 27-43.

708 Hamilton, E.H., Cleek, G.W. (1958) Properties of sodium titanium silicate glasses. *J. Res. Nat.*
709 *Bur. Stand.* **61**, 89-94.

710 Hammersley, A.P. (1997) *FIT2D: An Introduction and Overview*.

711 Hehlen, B., Courtens, E., Yamanaka, A., Inoue, K. (2002) Nature of the Boson peak of silica
712 glasses from hyper-Raman scattering. *J. Non-Cryst. Solids* **307-310**, 87-91.

713 Hehlen, B., Neuville, D.R. (2015) Raman Response of Network Modifier Cations in Aluminosilicate Glasses. *J. Phys. Chem. B* **119**, 4093-4098.

715 Henderson, G.S., Fleet, M.E. (1997) The structure of titanium silicate glasses investigated by Si
716 K-edge X-ray absorption spectroscopy. *J. Non-Cryst. Solids* **211**, 214-221.

717 Henderson, G.S., St-Amour, J.C. (2004) A Si K-edge XANES study of Ti containing
718 alkali/alkaline-earth silicate glasses. *Chem. Geol.* **213**, 31-40.

719 Hess, N., Su, Y., Balmer, M. (2001) Evidence of edge-sharing TiO₅ polyhedra in Ti-substituted
720 pollucite, CsTi_xAl_{1-x}Si₂O_{6+x/2}. *J. Phys. Chem. B* **105**, 6805-6811.

- 721 Hoppe, U., Brow, R., Tischendorf, B., Kriltz, A., Jovari, P., Schops, A., Hannon, A. (2007)
722 Structure of titanophosphate glasses studied by X-ray and neutron diffraction. *J. Non-*
723 *Cryst. Solids* **353**, 1802-1807.
- 724 Kajiwara, M. (1988) Formation and Crystallization of Al_2O_3 - TiO_2 - SiO_2 Glasses. *Glass Technol.*
725 **29**, 188-192.
- 726 Keen, D. (2001) A comparison of various commonly used correlation functions for describing
727 total scattering. *J. Appl. Cryst.* **34**, 172-177.
- 728 Kelly, S., Hesterburg, D., Ravel, B. (2008) Analysis of soils and minerals using X-ray absorption
729 spectroscopy, in: Ulery, A.L., Drees, L.R. (Eds.), *Methods of Soil Analysis Part 5:*
730 *Mineralogical Methods*. Soil Science Society of America, Inc., Madison, WI, pp. 387-
731 463.
- 732 Kirschen, M., Decapitani, C., Millot, F., Rifflet, J., Coutures, J.P. (1999) Immiscible silicate
733 liquids in the system SiO_2 - TiO_2 - Al_2O_3 . *Eur. J. Mineral.* **11**, 427-440.
- 734 Konishi, H., Yokoya, A., Shiwaku, H., Motohashi, H., Makita, T., Kashiara, Y., Hashimoto, S.,
735 Harami, T., Sasaki, T.A., Maeta, H., Ohno, H., Maezawa, H., Asaoka, S., Kanaya, N., Ito,
736 K., Usami, N., Kobayashi, K. (1996) Synchrotron radiation beamline to study radioactive
737 materials at the Photon factory. *Nucl. Instr. Methods A* **372**, 322-332.
- 738 Krawczynski, M.J., Sutton, S.R., Grove, T.L., Newville, M. (2009) Titanium oxidation state and
739 coordination in the lunar high-titanium glass source mantle, *Lunar and Planetary Science*
740 *Conference*. Lunar and Planetary Science Institute, Houston, TX.
- 741 Krzmanc, M., Dosler, U., Suvorov, D. (2012) Effect of a TiO_2 Nucleating Agent on the
742 Nucleation and Crystallization Behavior of MgO - B_2O_3 - SiO_2 Glass. *J. Am. Ceram. Soc.*
743 **95**, 1920-1926.
- 744 Lager, G.A., Armbruster, T., Ross, F.K., Rotella, F.J., Jorgensen, J.D. (1981) Neutron powder
745 diffraction study of defect spinel structures: Tetrahedrally coordinated Ti^{4+} in
746 $\text{Ni}_{2.62}\text{Ti}_{0.69}\text{O}_4$ and $\text{Ni}_{2.42}\text{Ti}_{0.74}\text{Si}_{0.05}\text{O}_4$. *J. Appl. Crystallogr.* **14**, 261-264.
- 747 Le Losq, C., Cicconi, M.R., Greaves, G.N., Neuville, D.R. (2019) Silicate Glasses, in:
748 Musgraves, J.D., Hu, J., Calvez, L. (Eds.), *Springer Handbook of Glass*. Springer, pp.
749 441-503.
- 750 Le Losq, C., Neuville, D.R. (2017) Molecular structure, configurational entropy and viscosity of
751 silicate melts: Link through the Adam and Gibbs theory of viscous flow. *J. Non-Cryst.*
752 *Solids* **463**, 175-188.
- 753 Lee, S., Stebbins, J. (2000) Al-O-Al and Si-O-Si sites in framework aluminosilicate glasses with
754 $\text{Si}/\text{Al}=1$: quantification of framework disorder. *J. Non-Cryst. Solids* **270**, 260-264.
- 755 Lee, S.M., Jo, Y.H., Kim, H.E., Mohanty, B.C., Cho, Y.S. (2012) Barium Neodymium Titanium
756 Borate Glass- Based High k Dielectrics. *J. Am. Ceram. Soc.* **95**, 1356-1359.
- 757 Limbach, R., Karlsson, S., Scannell, G., Mathew, R., Edén, M., Wondraczek, L. (2017) The
758 effect of TiO_2 on the structure of Na_2O - CaO - SiO_2 glasses and its implications for thermal
759 and mechanical properties. *J. Non-Cryst. Solids* **471**, 6-18.

Loewenstein, W. (1954) The distribution of aluminum in the tetrahedra of silicates and aluminates. *Am. Mineral.* **39**, 92-96.

Marcial, J., McCloy, J. (2019) Role of short range order on crystallization of tectosilicate glasses: A diffraction study. *J. Non-Cryst. Solids* **505**, 131-143.

McMillan, P. (1984) Structural studies of silicate glasses and melts: applications and limitations of Raman spectroscopy. *Am. Mineral.* **69**, 622-644.

Miyaji, F., Yoko, T., Kozuka, H., Sakka, S. (1991) Structure of Na₂O-2TiO₂ Glass. *J. Mater. Sci* **26**, 248-252.

Mumme, W.G., Wadsley, A.D. (1967) The crystal structure of NaTi₂Al₅O₁₂. *Acta Cryst.* **23**, 754-758.

Mysen, B., Neuville, D. (1995) Effect of temperature and TiO₂ content on the structure of Na₂Si₂O₅–Na₂Ti₂O₅ melts and glasses. *Geochim. Cosmochim. Acta* **59**, 325-342.

Mysen, B.O., Toplis, M.J. (2007) Structural behavior of Al³⁺ in peralkaline, metaluminous, and peraluminous silicate melts and glasses at ambient pressure. *Am. Mineral.* **92**, 933.

Mysen, B.O., Virgo, D., Seifert, F.A. (1982) The structure of silicate melts: Implications for chemical and physical properties of natural magma. *Rev. Geophys.* **20**, 353-383.

Nasu, H., Matsushita, O., Kamiya, K., Kobayashi, H., Kubodera, K.i. (1990) Third harmonic generation from Li₂O-TiO₂-TeO₂ glasses. *J. Non-Cryst. Solids* **124**, 275-277.

Neuefeind, J., Feygenson, M., Carruth, J., Hoffmann, R., Chipley, K.K. (2012) The Nanoscale Ordered Materials Diffractometer NOMAD at the Spallation Neutron Source SNS. *Nucl. Instrum. Methods Phys. Res. B* **287**, 68-75.

Neuville, D., Cormier, L., Flank, A.-M., Prado, R., Lagarde, P. (2004) Na K-edge XANES spectra of minerals and glasses. *Eur. J. Mineral.* **16**, 809-816.

Newville, M. (2001) IFEFFIT : interactive XAFS analysis and FEFF fitting. *J. Synchr. Rad.* **8**, 322-324.

Peterson, G.E., Kurkjian, C.R. (1972) Resolution of ⁴⁷Ti and ⁴⁹Ti hyperfine lines in glass. *Solid State Commun.* **11**, 1105-1107.

Rao, B. (1963) The dual role of titanium in the system K₂O-SiO₂-TiO₂. *Phys. Chem. Glasses* **4**, 22-34.

Rao, B.V.J. (1964) Properties and Structure of Glasses in the Binary Systems Alkali-TiO₂. *J. Am. Ceram. Soc.* **47**, 455-463.

Ravel, B., Newville, M. (2005a) ATHENA and ARTEMIS: Interactive graphical data analysis using IFEFFIT. *Phys. Scripta* **T115**, 1007-1010.

Ravel, B., Newville, M. (2005b) ATHENA, ARTEMIS, HEPHAESTUS: data analysis for X-ray absorption spectroscopy using IFEFFIT. *J. Synchr. Rad.* **12**, 537-541.

Richet, P., Mysen, B.O. (2019) *Silicate glasses and melts*, 1st ed. ed. Amsterdam, Netherlands : Elsevier, Amsterdam, Netherlands.

Romano, C., Paris, E., Poe, B., Giuli, G. (2000) Effect of aluminum on Ti-coordination in silicate glasses: A XANES study. *Am. Mineral.* **85**, 108-117.

799 Sabadel, J.C., Armand, P., Cachau-Herreillat, D., Baldeck, P., Doclot, O., Ibanez, A., Philippot,
800 E. (1997) Structural and Nonlinear Optical Characterizations of Tellurium Oxide-Based
801 Glasses: $\text{TeO}_2\text{--BaO--TiO}_2$. *J. Solid State Chem.* **132**, 411-419.

802 Sakka, S., Kozuka, H., Fukumi, K., Miyaji, F. (1990) Structures of gallate, aluminate and titanate
803 glasses. *J. Non-Cryst. Solids* **123**, 176-181.

804 Sakka, S., Miyaji, F., Fukumi, K. (1989) Structure of Binary $\text{K}_2\text{O--TiO}_2$ and $\text{Cs}_2\text{O--TiO}_2$ Glasses.
805 *J. Non-Cryst. Solids* **112**, 64-68.

806 Sears, V.F. (1992) Neutron scattering lengths and cross sections. *Neutron News* **3**, 26-37.

807 Sharma, S.K., Philpotts, J.A., Matson, D.W. (1985) Ring distributions in alkali- and alkaline-
808 earth aluminosilicate framework glasses- a Raman spectroscopic study. *J. Non-Cryst.*
809 *Solids* **71**, 403-410.

810 Soper, A. (2011) *GudrunN & GudrunX: Programs for correcting raw neutron and X-ray*
811 *diffraction data to differential scattering cross section.*

812 Soper, A.K. (2009) Empirical Potential Structure Refinement- EPSR Shell.

813 Virgo, D., Mysen, B.O., Kushiro, I. (1980) Anionic Constitution of 1-Atmosphere Silicate Melts:
814 Implications for the Structure of Igneous Melts. *Science* **208**, 1371-1373.

815 Williams, Q., Manghnani, M.H., Matsui, T. (2019) The effect of coordination changes on the
816 bulk moduli of amorphous silicates-the $\text{SiO}_2\text{--TiO}_2$ system as a test case. *Am. Mineral.*
817 **104**, 679-685.

818 Woicik, J.C., Ravel, B., Fischer, D.A., Newburgh, W.J. (2010) Performance of a four-element Si
819 drift detector for X-ray absorption fine-structure spectroscopy: resolution, maximum
820 count rate, and dead-time correction with incorporation into the ATHENA data analysis
821 software. *J. Synchr. Rad.* **17**, 409-413.

822 Yamamoto, T. (2008) Assignment of pre-edge peaks in K-edge -ray absorption spectra of 3d
823 transition metal compounds: electric dipole or quadrupole? *X-Ray Spectrom.* **37**, 572-584.

824 Yarker, C.A., Johnson, P.A.V., Wright, A.C., Wong, J., Gregor, R.B., Lytle, F.W., Sinclair,
825 R.N. (1986) Neutron diffraction and EXAFS evidence for TiO_5 units in vitreous $\text{K}_2\text{O--}$
826 $\text{TiO}_2\text{--}2\text{SiO}_2$. *J. Non-Cryst. Solids* **79**, 117-136.

827 Yu, J., Kohara, S., Itoh, K., Nozawa, S., Miyoshi, S., Arai, Y., Masuno, A., Taniguchi, H., Itoh,
828 M., Takata, M., Fukunaga, T., Koshihara, S., Kuroiwa, Y., Yoda, S. (2009)
829 Comprehensive Structural Study of Glassy and Metastable Crystalline BaTi_2O_5 . *Chem.*
830 *Mater.* **21**, 259-263.

831 Ziadi, A., Hillebrecht, H., Thiele, G., Elouadi, B. (1996) Crystal Structure of Orthorhombic LT-
832 $\text{Na}_2\text{TiSiO}_5$ and Its Relation to the Tetragonal HT-Form. *J. Solid State Chem.* **123**, 324-
833 330.

837 Table 1. Sample names, compositions (nominal and analyzed), and mass densities of glasses used in this study
838

Sample	Composition	Oxides (mol%) nominal				Oxides (wt%) analyzed				Density, Archim. (g/cm ³)	Density, Pycnom. (g/cm ³)
		Na ₂ O	Al ₂ O ₃	SiO ₂	TiO ₂	Na ₂ O	Al ₂ O ₃	SiO ₂	TiO ₂		
NAS	NaAlSiO ₄	25.0	25.0	50.0	0.0	21.476(71)	36.374(669)	39.775(1025)	0.007(16)	2.490(1)	2.4923
0.025Ti-NAS	NaAlTi _{0.025} Si _{0.975} O ₄	25.0	25.0	48.75	1.25	19.702(132)	35.864(67)	39.802(337)	1.427(53)	2.500(2)	2.5111
0.050Ti-NAS	NaAlTi _{0.050} Si _{0.950} O ₄	25.0	25.0	47.5	2.5	19.681(169)	36.060(262)	38.994(338)	2.846(46)	2.496(4)	2.4923
0.075Ti-NAS	NaAlTi _{0.075} Si _{0.925} O ₄	25.0	25.0	46.25	3.75	19.512(128)	35.544(62)	38.078(275)	4.294(56)	2.510 (1)	2.5083
0.1Ti-NAS	NaAlTi _{0.1} Si _{0.9} O ₄	25.0	25.0	45.0	5.0	18.941(53)	35.204(203)	37.182(616)	5.708(49)	2.515 (5)	2.5016
0.2Ti-NAS	NaAlTi _{0.2} Si _{0.8} O ₄	25.0	25.0	40.0	10.0	18.247(210)	35.173(76)	32.915(314)	11.162(123)	2.559(1)	2.5503
0.3Ti-NAS	NaAlTi _{0.3} Si _{0.7} O ₄	25.0	25.0	35.0	15.0	17.622(171)	35.147(209)	29.066(444)	16.643(102)	2.614(3)	2.6048
0.4Ti-NAS*	NaAlTi _{0.4} Si _{0.6} O ₄	25.0	25.0	30.0	20.0	n/a	n/a	n/a	n/a	n/a	n/a
0.5Ti-NAS*	NaAlTi _{0.5} Si _{0.5} O ₄	25.0	25.0	25.0	25.0	n/a	n/a	n/a	n/a	n/a	n/a
NAT*	NaTiSiO ₄	25.0	25.0	0.0	50.0	n/a	n/a	n/a	n/a	n/a	n/a

839 *Resulted in crystallization upon quench; did not produce a single-phase glass. Therefore, they were not analyzed by
840 EPMA (n/a). Neither were their density.
841

842 Table 2. A list of samples and the PDF analysis experiments performed for each. See Appendix for description of
843 the lab-scale xPDF measurements
844

Sample	Neutron PDF	Synchrotron xPDF	Lab-scale xPDF	EPSR
NAS	x	x	x	x
0.025Ti	x	x	x	
0.050Ti	x	x	x	
0.075Ti	x	x	x	
0.1Ti	x	x	x	x
0.2Ti	x	x	x	x
0.3Ti	x		x	x

845
846 Table 3. Potentials used in EPSR modeling.
847

Atom Type	ε (kJ/mole)	σ (Å)	M (amu)	q (e)	Reference
Si	0.8	0.76	28	4.0	(Bernasconi et al., 2012)
Al	0.8	1.2	27	3.0	(Bernasconi et al., 2012)
Na	0.8	2.3	23	1.0	(Bernasconi et al., 2012)
Ti	2.23	1.31	48	4.0	(Alderman et al., 2014)
O	0.65	3.69	16	-2.0	(Bernasconi et al., 2016; Bernasconi et al., 2012)

848
849

Table 4. Atom box parameters used in EPSR modeling. Densities shown are from pycnometry

Sample	ρ (g/cm ³)	Na	Al	Si	Ti	O
NAS	2.4923	500	500	500	0	2000
0.1Ti-NAS	2.5016	500	500	450	50	2000
0.2Ti-NAS	2.5503	500	500	400	100	2000
0.3Ti-NAS	2.6048	500	500	350	150	2000

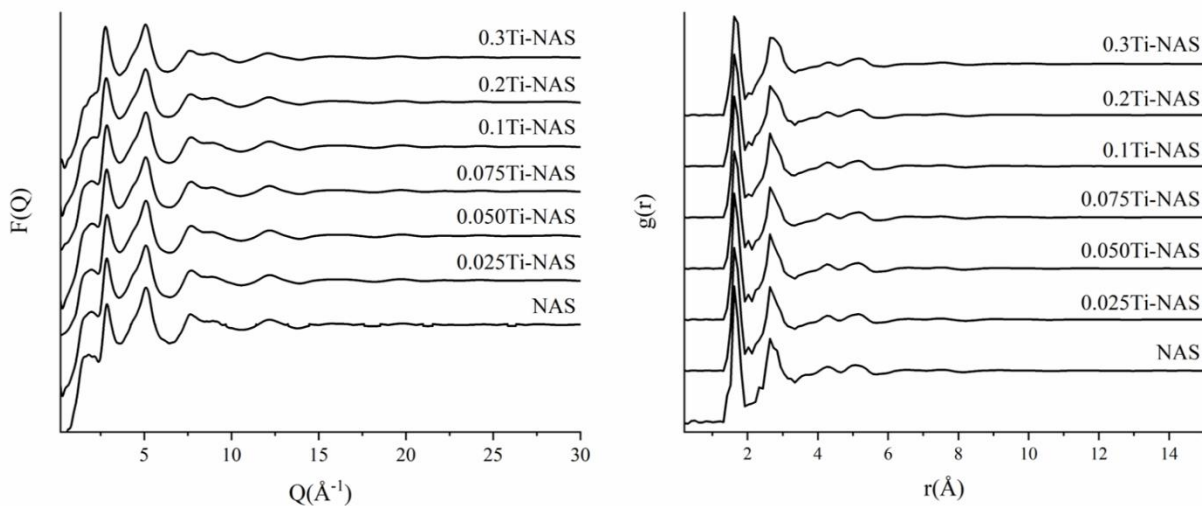
Table 5. Coordination numbers, and standard deviations, as calculated via EPSR and (CrystalMaker), shown in parentheses, through a user defined bond distance window. Distance windows used in the calculation, in Å, are shown as determined through partial g(r)'s.

Sample	Average Coordination Number			
	Al-O	Na-O	Si-O	Ti-O
NAS	4.02±0.023	6.09±0.94	3.95±0.22	-
0.1Ti-NAS	3.93±0.28 (3.65±0.65)	6.23±1.03 (5.53±1.52)	3.94±0.23 (3.66±0.64)	4.14±0.34 (3.88±0.68)
0.2Ti-NAS	3.95±0.25 (3.67±0.62)	6.50±0.99 (5.85±1.48)	3.93±0.206 (3.66±0.64)	3.98±0.20 (3.78±0.58)
0.3Ti-NAS	3.99±0.19 (3.71±0.62)	5.46±1.03 (4.83±1.14)	3.95±0.21 (3.73±0.56)	4.12±0.33 (3.88±0.67)
Distance Window (Å)	1.5-2.3	2.0-3.2	1.3-2.0	1.6-2.2

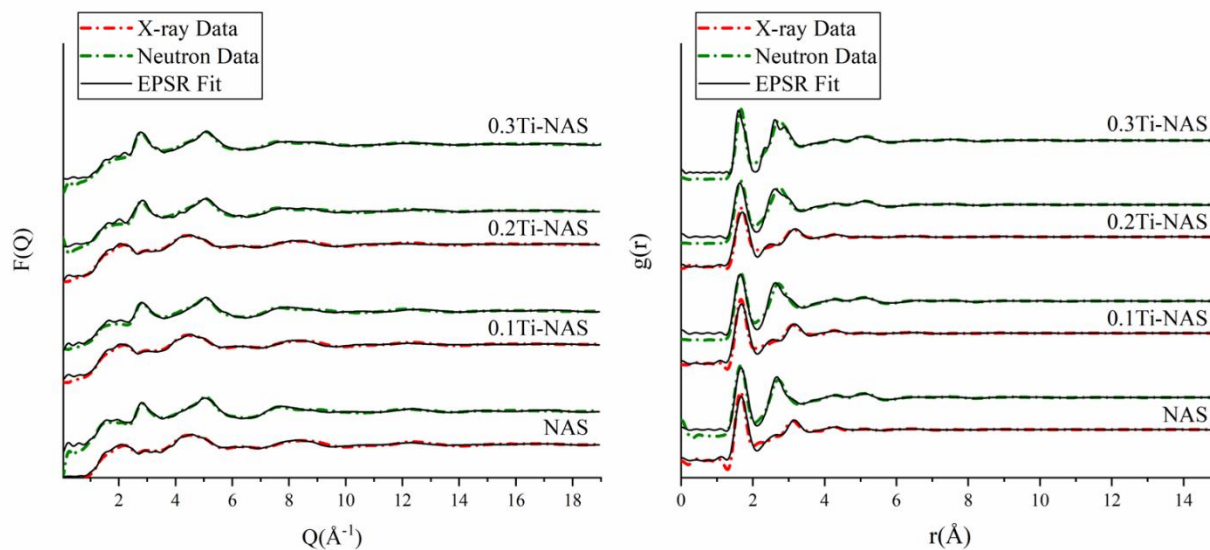
Table 6. Structural parameters for Ti-containing glasses obtained from modeling Ti K-edge EXAFS. R_{Ti-i} is the average interatomic distance for a given Ti-i pair, σ_i^2 is the EXAFS Debye-Waller factor (estimated from the distribution of bond length) and N_{Ti-O} is the refined number of scatterers in the first oxygen coordination shell which was allowed to refine; the number of scatterers in all other shells were fixed during the fits to 2 each for Al, Ti, and Si. The amplitude reduction factor (S_0^2), determined from the fitting of the TiO₂ rutile reference, was fixed at $S_0^2 = 0.65$. BVS is the bond valence sum for the first oxygen coordination shells.

	0.075Ti-NAS		0.1Ti-NAS		0.2Ti-NAS		0.3Ti-NAS	
	±		±		±		±	
E_0 (eV)	0.72	3.54	-0.35	2.15	-2.9	1.7	-3.09	1.80
R_{Ti-O} (Å)	1.85	0.03	1.85	0.02	1.84	0.01	1.85	0.01
N_{Ti-O}	3.87	0.74	3.85	0.46	3.99	0.45	4.11	0.47
σ_O^2 (Å ²)	0.009	0.003	0.007	0.002	0.006	0.012	0.008	0.002
R_{Ti-Ti} (Å)	2.46	0.03	2.46	0.02	3.02	0.05	3.02	0.05
σ_{Ti}^2 (Å ²)	0.013	0.003	0.017	0.004	0.004	0.007	0.004	0.006
R_{Ti-Al} (Å)	2.96	0.09	3.00	0.08	2.76	0.04	2.76	0.04
σ_{Al}^2 (Å ²)	0.016	0.014	0.017	0.011	0.014	0.007	0.013	0.006
R_{Ti-Si} (Å)	3.25	0.04	3.25	0.03	2.99	0.06	2.98	0.05
σ_{Si}^2 (Å ²)	0.005	0.005	0.005	0.003	0.001	0.007	0.001	0.005
R factor	0.037	-	0.015	-	0.018	-	0.018	-
BVS (v.u.)	3.52	1.03	3.50	0.23	3.73	0.53	3.74	0.54

867 Figures



869 Figure 1. Experimental $F(Q)$ and $g(r)$ as obtained through neutron total scattering experiments.



872 Figure 2. Comparison of experimental and EPSR simulation $F(Q)$ (left) and $g(r)$ (right) for neutron and X-ray data.

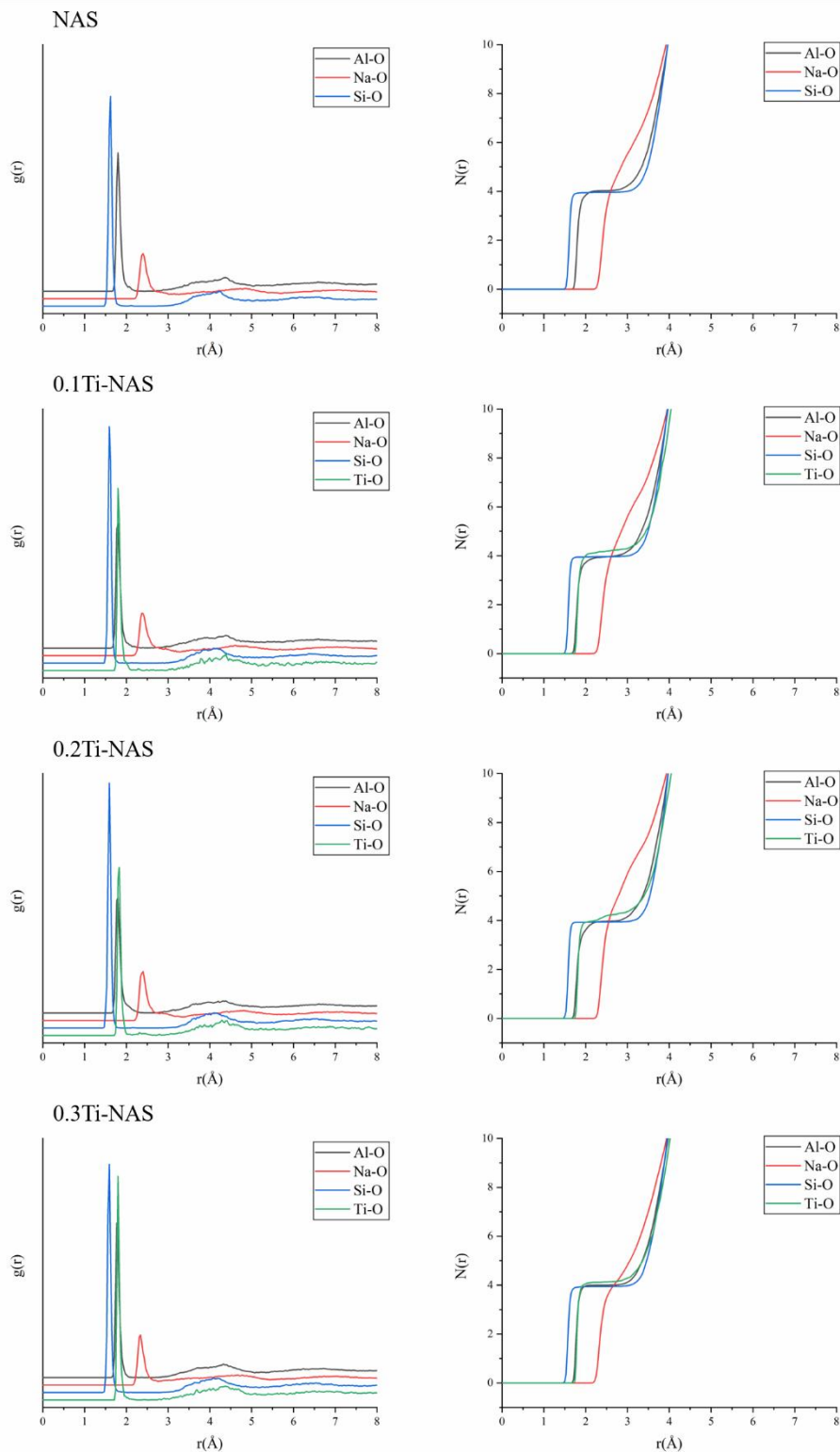


Figure 3. Partial (deconvoluted) $g(r)$ and $N(r)$ plots obtained through EPSR simulation. The inflection/plateau in the $N(r)$ plots gives the average coordination number of the species.

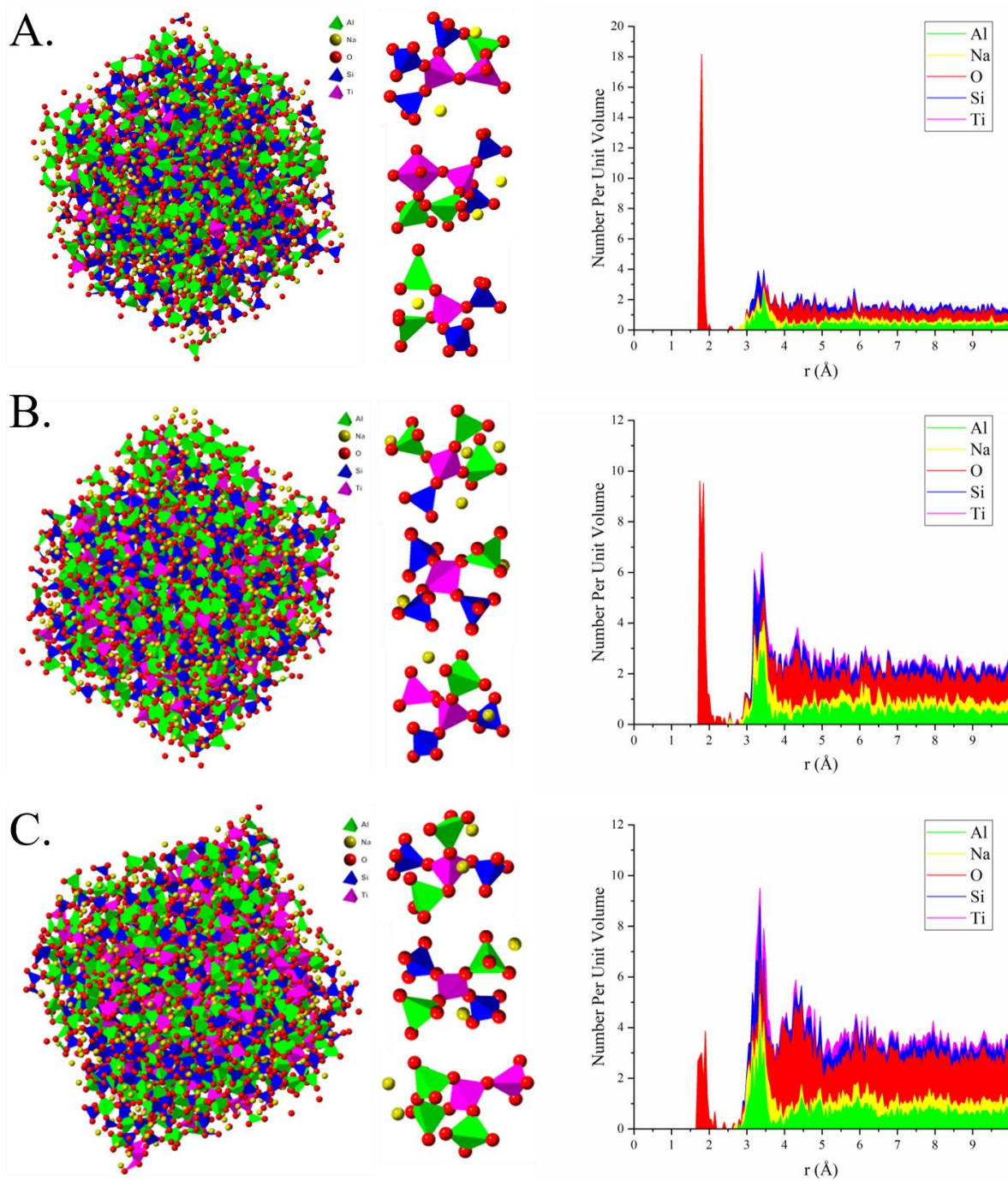


Figure 4. Exported atom models, with sample Ti environments, from EPSR and the subsequent bond distributions from CrystalMaker. Atom models for A.) 0.1Ti-NAS; B.) 0.2Ti-NAS; C.) 0.3Ti-NAS.

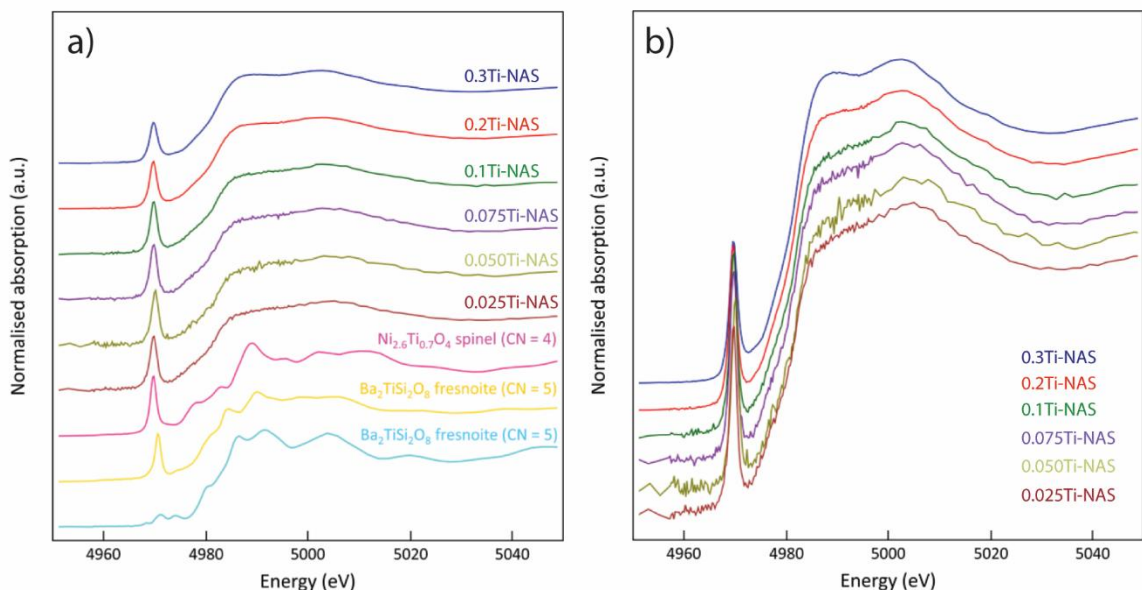


Figure 5. XANES region measurements for the Ti K-edge XAS. a.) Showing standards with all glasses. Standards shown were measured at KEK in transmission. Glasses shown were measured at NSLS-II in transmission, and are representative of the other measurements of the glasses at KEK in transmission and NSLS-II in fluorescence. b.) Overlay of glasses showing progressive changes in the ~4985 – 5010 eV range.

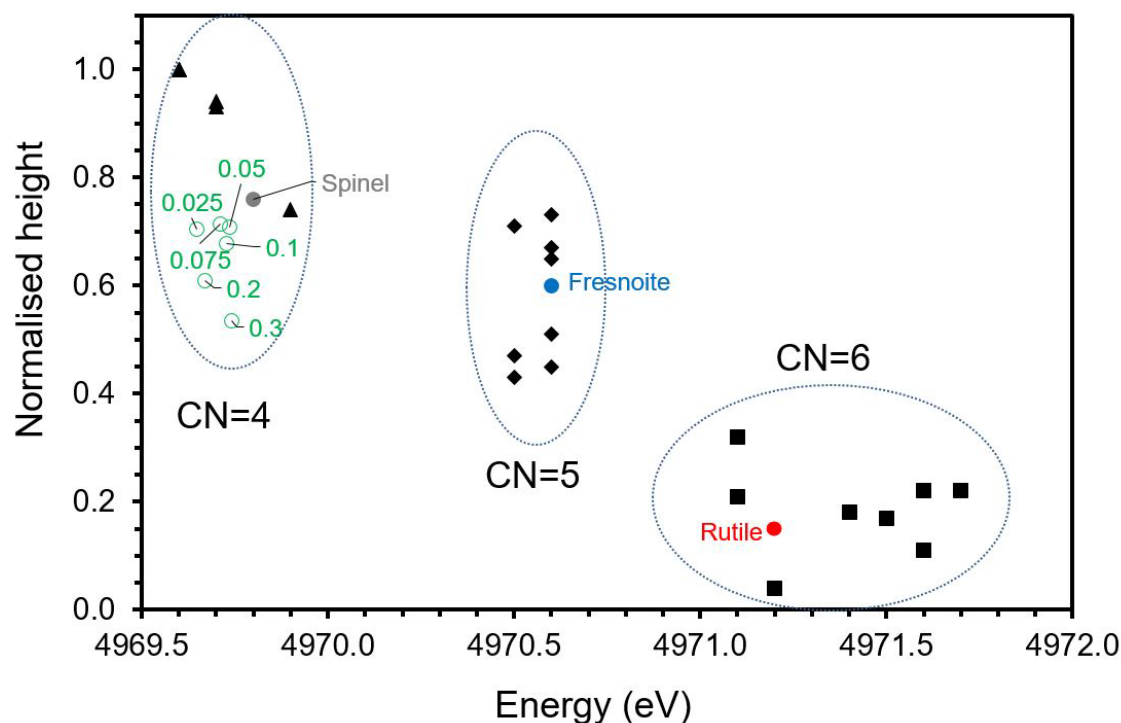
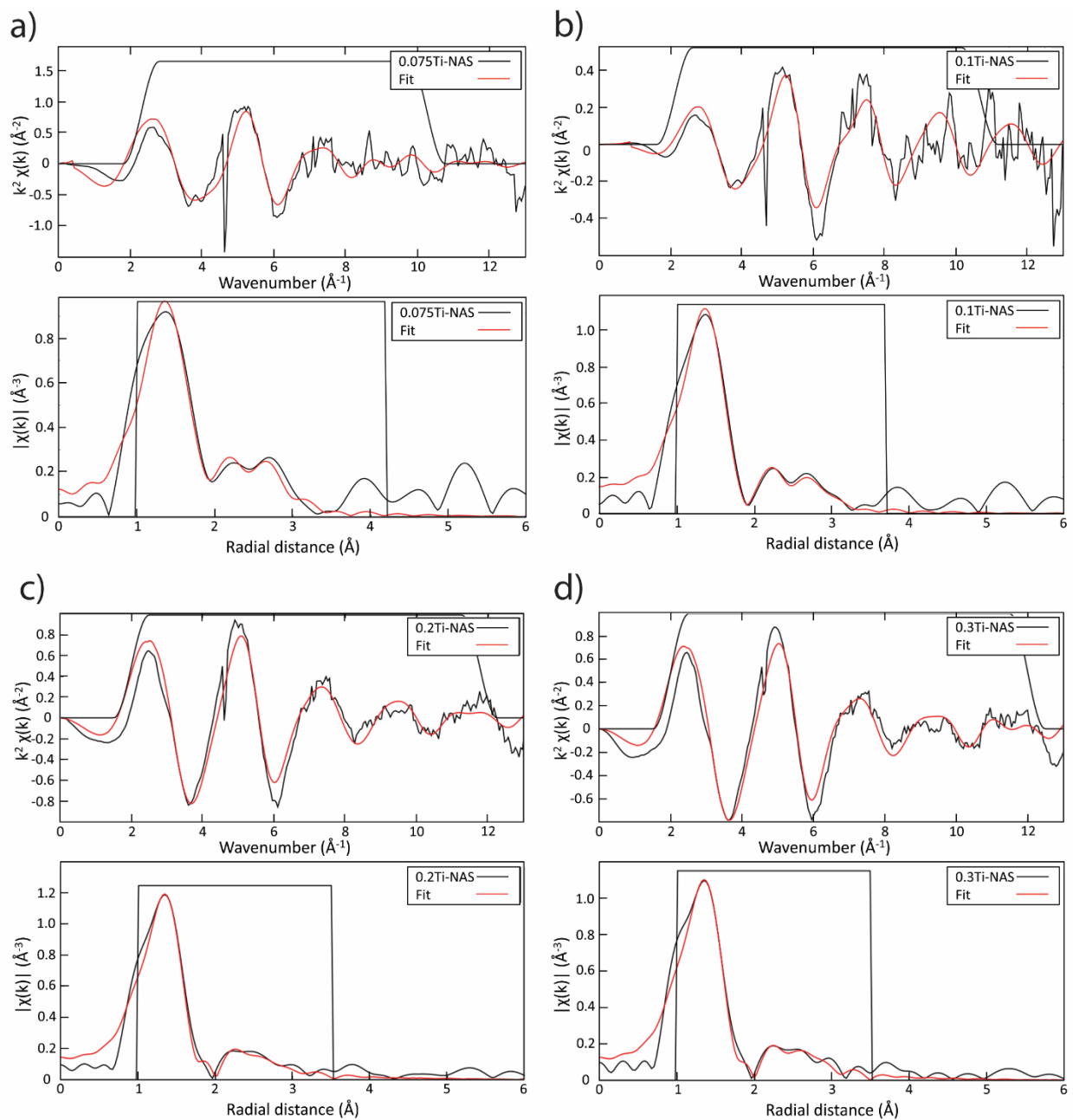


Figure 6. Energy versus normalized height for the crystalline standards [labeled: rutile, (TiO₂), fresnoite, (Ba₂TiSi₂O₈), spinel, (Ni_{2.6}Ti_{0.7}O₄)], the glasses, and other crystalline materials having characteristic pre-edge features (from Farges et al (Farges et al., 1996c)). Data obtained for standards at KEK in transmission, and for glasses at NSLS-II (average of fits to transmission and fluorescence pre-edge data). For simplicity in the figure, the ‘Ti-NAS’ is eliminated from the sample names.



896 Figure. 7. EXAFS fits for a.) 0.075Ti-NAS; b.) 0.1Ti-NAS; c.) 0.2Ti-NAS; d.) 0.3Ti-NAS.

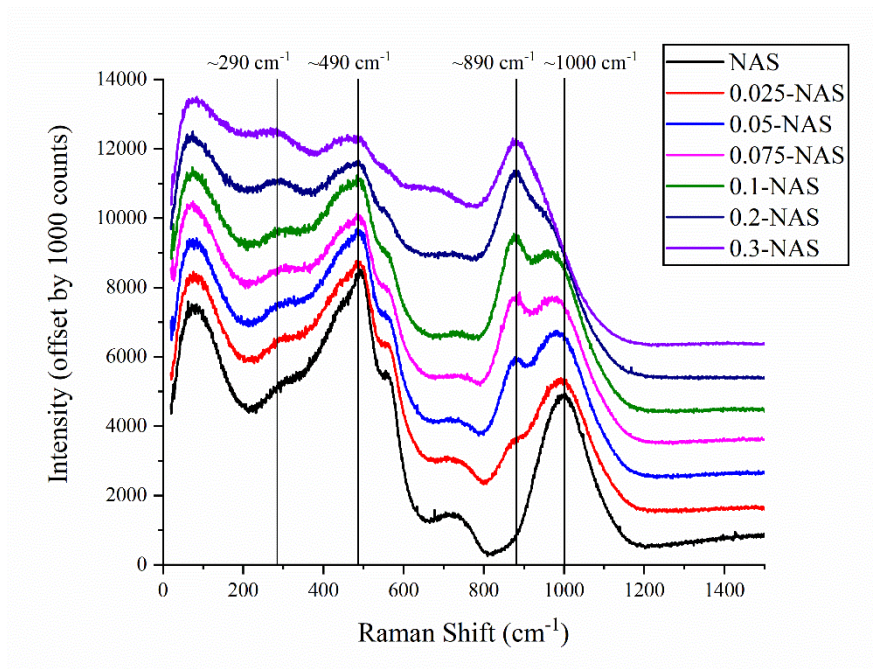


Figure 8. Raman spectra of Ti-NAS glass without any background subtraction or normalization; spectra are offset for clarity

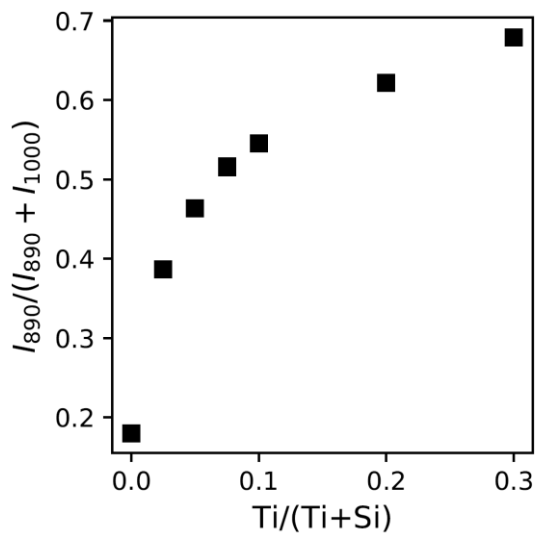


Figure 9. Relative intensities of the 890 cm⁻¹ Raman bands to the 1000 cm⁻¹ bands of the glasses as a function of the Ti/(Ti+Si) ratio in the glass.

Declaration of interests

☒ The authors declare that they have no known competing financial interests or personal relationships that could have appeared to influence the work reported in this paper.

☐ The authors declare the following financial interests/personal relationships which may be considered as potential competing interests: